How Does Solar Attenuation Depth Affect the Ocean Mixed Layer? Water Turbidity and Atmospheric Forcing Impacts on the Simulation of Seasonal Mixed Layer Variability in the Turbid Black Sea[*]

A. Birol Kara, Alan J. Wallcraft, and Harley E. Hurlburt

Oceanography Division, Naval Research Laboratory, Stennis Space Center, Mississippi

ABSTRACT

A fine-resolution ($\approx$3.2 km) Hybrid Coordinate Ocean Model (HYCOM) is used to investigate the impact of solar radiation attenuation with depth on the predictions of monthly mean sea surface height (SSH), mixed layer depth (MLD), buoyancy and heat fluxes, and near-sea surface circulation as well. The model uses spatially and temporally varying attenuation of photosynthetically available radiation (k_{PAR}) climatologies as processed from the remotely sensed Sea-Viewing Wide Field-of-View Sensor (SeaWiFS) to take water turbidity into account in the Black Sea. An examination of the k_{PAR} climatology reveals a strong seasonal cycle in the water turbidity, with a basin-averaged annual climatological mean value of 0.19 m^{-1} over the Black Sea. Climatologically forced HYCOM simulations demonstrate that shortwave radiation below the mixed layer can be quite different based on the water turbidity, thereby affecting prediction of upper-ocean quantities in the Black Sea. The clear water constant solar attenuation depth assumption results in relatively deeper MLD (e.g., $\approx$+15 m in winter) in comparison to standard simulations due to the unrealistically large amount of shortwave radiation below the mixed layer, up to 100 W m^{-2} during April to October. Such unrealistic sub–mixed layer heating causes weaker stratification at the base of the mixed layer. The buoyancy gain associated with high solar heating in summer effectively stabilizes the upper ocean producing shallow mixed layers and elevated SSH over the most of the Black Sea. In particular, the increased stability resulting from the water turbidity reduces vertical mixing in the upper ocean and causes changes in surface-layer currents, especially in the easternmost part of the Black Sea. Monthly mean SSH anomalies from the climatologically forced HYCOM simulations were evaluated against a monthly mean SSH anomaly climatology, which was constructed using satellite altimeter data from TOPEX/ Poseidon (T/P), *Geosat* Follow-On (GFO), and the *Earth Remote Sensing Satellite-2* (*ERS-2*) over 1993–2002. Model–data comparisons show that the basin-averaged root-mean-square (rms) difference is $\approx$4 cm between the satellite-based SSH climatology and that obtained from HYCOM simulations using spatial and temporal k_{PAR} fields. In contrast, when all solar radiation is absorbed at the sea surface or clear water constant solar attenuation depth values of 16.7 m are used in the model simulations, the basin-averaged SSH rms difference with respect to the climatology is $\approx$6 cm ($\approx$50% more). This demonstrates positive impact from using monthly varying solar attenuation depths in simulating upper-ocean quantities in the Black Sea. The monthly mean k_{PAR} and SSH anomaly climatologies presented in this paper can also be used for other Black Sea studies.

1. Introduction and motivation

The available oceanographic survey data is insufficient to describe upper-ocean quantities in the Black Sea, in detail. There are some observational studies (e.g., Oguz and Besiktepe 1999; Zatsepin et al. 2003) which described upper-ocean circulation in the Black Sea but the datasets reported from these studies had limited spatial and temporal scales. Thus, ocean general circulation models (OGCMs) are particularly useful in compensating for the sparseness of the oceanic observations and in providing a comprehensive picture of upper-ocean features on a wide variety of temporal and spatial scales in the Black Sea.

In this paper, we use a fine-resolution ($\approx$3.2 km) Hybrid Coordinate Ocean Model (HYCOM) for the Black Sea (Kara et al. 2005a). The model combines the advantages of the isopycnal, σ and partial-cell z-level coordinates within a single framework to allow the optimal coordinate choice in simulating coastal and open-ocean circulation features of the Black Sea. The hybrid coordinate approach in ocean modeling has been developed to handle the degeneracy of the isopycnic coordinate representation in unstratified or convectively unstable water columns (Bleck 2002). The use of fixed-depth z-level or terrain-following σ coordinates in the upper ocean allows the formulation of turbulent near-

Corresponding author address: A. Birol Kara, Naval Research Laboratory, Code 7320, Stennis Space Center, MS 39529-5004. E-mail: kara@nrlssc.navy.mil

surface mixing as in the K-Profile-Parameterization (KPP) theory (Large et al. 1997). The KPP is a first-order turbulence closure ocean surface boundary layer model that is intermediate in computational complexity between bulk mixed layer models and second-order turbulence closures, and it is relatively insensitive to low vertical resolution.

The vertical distribution of shortwave radiation within the upper ocean becomes a critical issue in predicting sea surface circulation and sea surface temperature in the Black Sea as shown by Kara et al. 2005b; (see related information in Kara et al. 2005a) who used HYCOM with the KPP mixed layer model. The reason is that shortwave radiation can penetrate below the mixed layer even under turbid conditions because the mixed layer can be very shallow in this region, resulting in destabilization of the thermal stratification. Thus, specific attention must be given to subsurface heating parameterization in an OGCM with a mixed layer. However, earlier OGCM studies in the Black Sea were limited to some extent by lack of spatial and temporal water turbidity fields. The effects of turbidity and how it was treated in the model are not mentioned either (e.g., Oguz and Malanotte-Rizzoli 1996; Stanev and Staneva 2001; Staneva et al. 2001). A few remote-sensing studies based on the TOPEX/Poseidon (T/P) altimetry were used in explaining Black Sea surface circulation (Korotaev et al. 1998); however, those studies were mainly observational and did not consider water turbidity effects on the circulation directly. With fine vertical grid spacing near the surface ($\leq$3 m) in HYCOM shortwave radiation attenuation with depth through water turbidity can be treated as a two-band spectrum, a red spectrum for the surface layers and a blue spectrum for deeper levels.

The major purposes of this paper are to (i) present the satellite-based monthly mean k_{PAR} climatology for use in OGCM applications and biological studies in the Black Sea, (ii) examine predictions of upper-ocean quantities from HYCOM with respect to net heat and buoyancy fluxes using the monthly k_{PAR} climatology, a subject neither observational studies nor fine-resolution eddy-resolving OGCM studies have investigated previously (Kara et al. 2005a examined annual mean), and (iii) validate model simulations of climatological seasonal variability. Specific attention is given to predictions of mixed layer depth (MLD), sea surface height (SSH), and surface circulation. In this paper, we do not explicitly investigate the dynamics of eddy formation or surface circulation but concentrate on the direct effects of water turbidity on mixed layer features. Another major purpose of this paper is to present a monthly mean SSH climatology constructed from satellite altimeter data for the Black Sea during 1993–2002, which is later used for the model validation. The altimeter data include ground tracks from three satellite systems: 1) The joint National Aeronautics and Space Administration (NASA) French TOPEX/Poseidon (T/P), 2) U.S. Navy's *Geosat*

Follow-On (GFO), and 3) The European Space Agency's *Earth Remote-Sensing Satellite-2* (*ERS-2*).

In section 2, spatial and temporal variability of k_{PAR} fields are introduced, as well as the relationship between attenuation depth and MLD. In section 3, a brief description of the OGCM used in this paper is given. In section 4, the Black Sea model setup is discussed along with atmospheric forcing fields used in the simulations. In section 5, sensitivity of upper-ocean quantities to water turbidity over the annual cycle is investigated in the light of subsurface heating. In section 6, detailed model–data comparisons are presented using a monthly SSH anomaly climatology with respect to the annual mean which is constructed from satellite altimeter data over a 10-yr period (1993–2002).

2. Monthly turbidity climatology in the Black Sea

The Black Sea (Fig. 1) is a very turbid region as discussed in Kara et al. 2005a, who introduced the annual mean attenuation depth climatology. Here we examine the climatological monthly variability of the attenuation depths which will be used in the model simulations. The climatology was constructed using daily mean attenuation coefficient data at 490 nm (k_{490}) obtained from the remotely sensed Sea-Viewing Wide Field-of-view Sensor (SeaWiFS) project (McClain et al. 1998) during 1 October 1997–31 December 2001. The original daily mean k_{490} dataset contained data voids because of cloud coverage and infrequent sampling by satellite sensors, as well as noise due to sensor limitations. After temporal filling using a one-dimensional periodic cubic spline, the remaining data voids were replaced by applying a statistical interpolation (Daley 1991) in space for each individual monthly mean, with an exponential correlation function assumed for the covariance. To obtain the monthly mean turbidity fields, k_{PAR} values that have a dependence upon a reference wavelength were used. Such a relationship has been determined through a set of regressions (Zaneveld et al. 1993).

The monthly mean k_{PAR} was computed from the k_{490} and spatially interpolated for use in the model as shown in Fig. 2. Attenuation depth values generally range from $\approx$3 to 10 m (k_{PAR} values of $\approx$0.3 to 0.1 m^{-1}, respectively). In comparison to the interior of the Black Sea, the coastal waters typically have small k_{PAR} values (i.e., less turbidity), especially in spring and summer. The basin-averaged monthly mean k_{PAR} values (Fig. 3) illustrate the distinct regimes of the lower spring–summer and higher fall–winter turbidity with an annual mean value of 0.19 m^{-1}.

The pattern of turbidity in the Black Sea can be roughly explained as follows: The high turbidity in the western part of the basin is due to rivers. In the central and eastern Black Sea turbidity is higher in the interior and lower near the boundaries due to the cyclonic interior circulation. This pattern is influenced by advection and
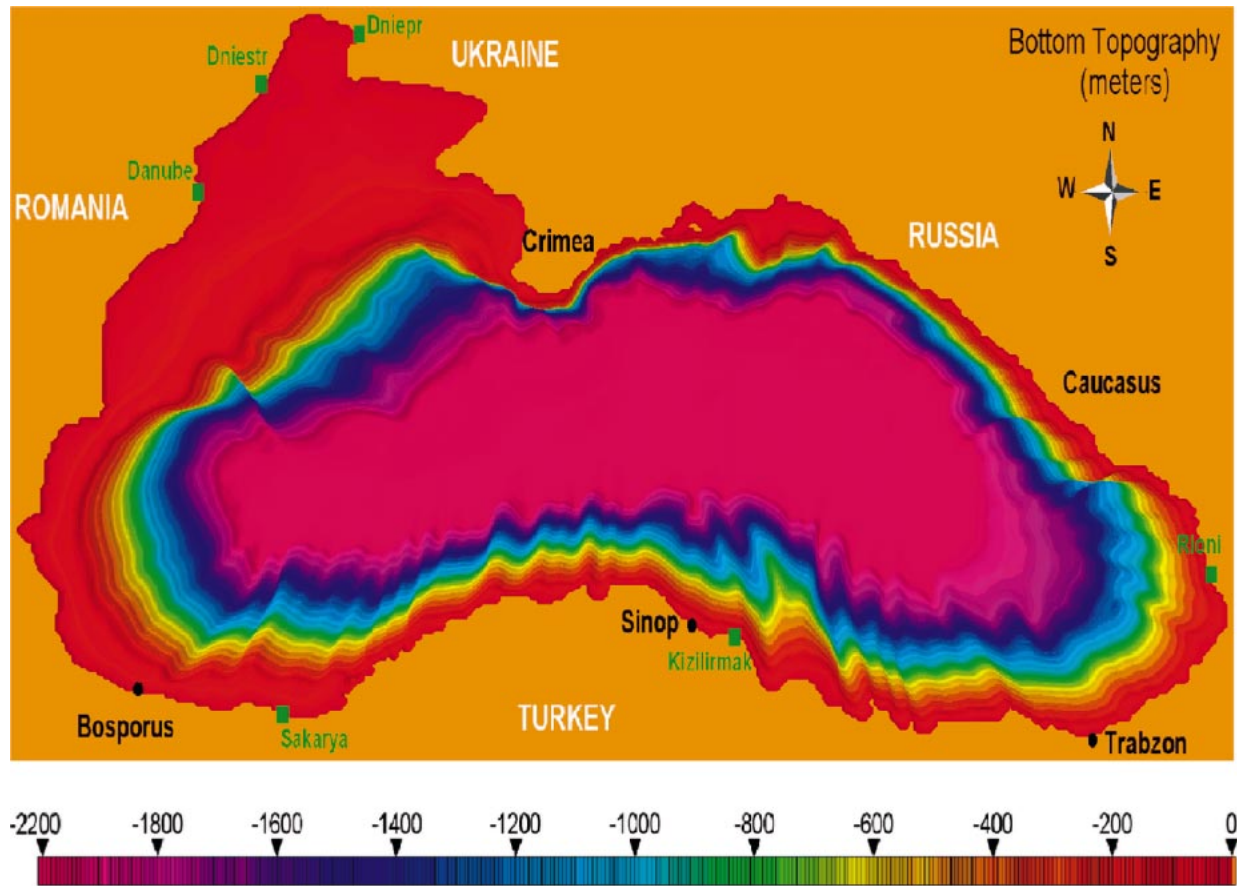
FIG. 1. The Black Sea bottom topography (m) used in the HYCOM simulations. It was constructed from the DBDB-V dataset obtained from NAVOCEANO. In the Black Sea it is the DBDB-1.0, that is, 1′ (1 min) resolution. After interpolation to the Black Sea model grid, the final topography was also smoothed twice with a nine-point smoother to reduce topographic energy generation poorly resolved by the model grids. Only major rivers named on the map (in green) are used in the model simulations. Two coastal cities, Trabzon and Sinop, used in the text are also shown (in black) as well as the Crimea and Caucasus Peninsulas. The Bosporus is considered a negative precipitation field to close the evaporation minus precipitation budget in the Black Sea. The net freshwater balance (P_{net}) in the model is expressed as $P_{net} = E - P + P_{River} + P_{Bosp.}$, where E is evaporation, P is precipitation due to rain or snow, P_{River} is due to rivers parameterized as precipitation, and $P_{Bosp.}$ is ''negative precipitation'' (i.e., evaporation) due to the transport from the Bosporus Strait.

by the associated interior upwarping of the isopycnals (which gives interior upwelling) and downwarping near the boundaries (which gives downwelling). Because of the strong, shallow pycnocline, the associated overturning is shallow and very effective in bringing nutrient-rich water into the euphotic zone in the interior of the basin.

The monthly time series of k_{PAR} at some selected locations (Fig. 4) clearly reveal wide variations in the amplitude of the annual cycle in the Black Sea. However, k_{PAR} values in summer are generally smaller than in other months, consistent with the areal means. At some locations, k_{PAR} can be very large, for example, 0.48 m^{-1} and 0.34 m^{-1} at (41.4°N, 29.1°E) and (45.5°N, 31.0°E), respectively. It is emphasized that we are interested in regions with relatively small k_{PAR} values because they may induce a change in upper-ocean quantities. All large k_{PAR} values (i.e., $k_{PAR} > 0.30$ m^{-1}) result

in complete absorption of the solar radiation within the mixed layer as shown in Kara et al. (2005a).

From the numerical ocean modeling point of view, the greatest interest is in situations where subsurface heating can occur below the mixed layer. Thus, we provide a brief explanation about shortwave radiation, MLD, and maximum PAR absorption depth (D_C), all of which are directly related to the subsurface heating and sub–mixed layer heat budget. Climatological monthly means of these quantities are shown in Fig. 5 for February and June. In addition, basin-averaged climatological means of these quantities are given in Table 1 by month. The MLD is defined as the depth at the base of an isopycnal layer, where the density has changed by a variable amount, $\Delta \sigma_t = \sigma_t(T + \Delta T, S, 0) - \sigma_t(T, S, 0)$, from the density at a reference depth of 3 m based on a chosen ΔT value (Kara et al. 2000). In this representation of MLD, S is the salinity and T is the tem-
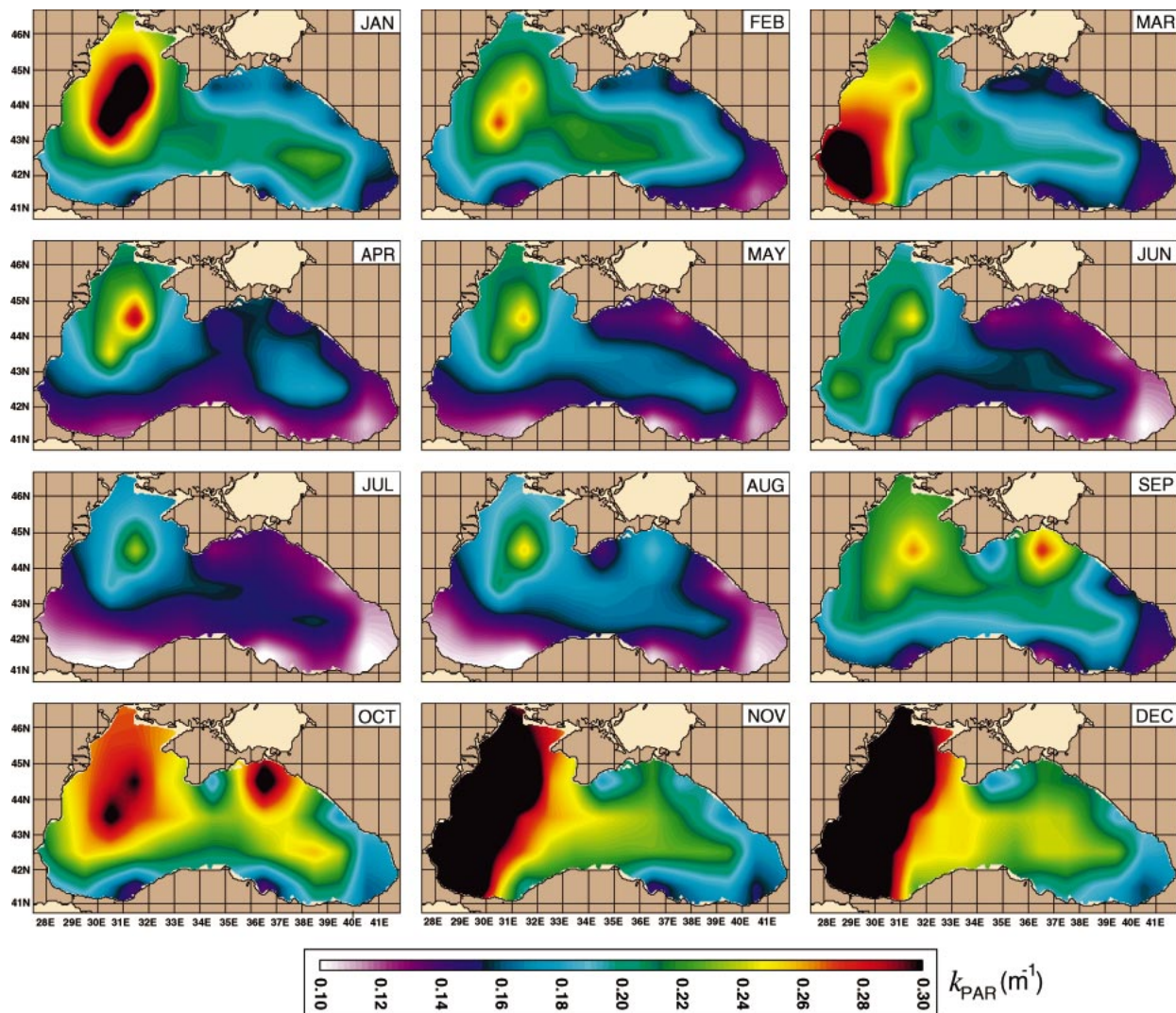
FIG. 2. Climatological monthly mean attenuation of photosynthetically available radiation (k_{PAR}) over the Black Sea. These fields were processed from the remotely sensed monthly attenuation coefficient at 490 nm (k_{490}), which was acquired from a daily mean SeaWiFS dataset covering 1 Oct 1997–31 Dec 2001. It is noted that the original k_{490} dataset from SeaWiFS had some data voids. The data filling of the k_{490} data using a statistical interpolation proceeds by searching for data voids along latitude transects. Searches along longitude proceed from west to east, and then from east to west. An interpolating grid box of 5 $\times$ 5 centered at the data void is used for the statistical interpolation. The climatology presented here has high spatial resolution of 9 km ($\approx \frac{1}{12}$°) over the Black Sea. As seen, the easternmost part of the Black Sea has the lowest turbidity but the western part of the region ($\approx$west of 33°E) has the largest turbidity due to rivers. This is generally true for all months. Regions where turbidity is the largest are usually in the western part especially during Nov and Dec.

perature. While Kara et al. (2003a) reports that the chosen optimal temperature difference (ΔT) should be 0.8°C, we use a ΔT value of 0.5°C. The reason is that there is strong density stratification in the Black Sea. The maximum PAR absorption depth, defined as $D_C = \ln(0.01)/k_{PAR}$, represents the maximum depth for solar heating of the upper ocean (Lalli and Parsons 1997). The k_{PAR} values obtained from SeaWiFS were used to calculate D_C to provide general information about the layer extending from the surface to the depth of the 1% light level. Shortwave radiation climatologies at the sea surface were constructed from the 1.125° $\times$ 1.125° European Centre for Medium-Range Weather Forecasts

(ECMWF) Re-Analysis (ERA) product (Gibson et al. 1997) during 1979–93, and from the 1.0° $\times$ 1.0° Fleet Numerical Meteorology and Oceanography Center (FNMOC) Navy Operational Global Atmospheric Prediction System (NOGAPS) archived operational product (Rosmond et al. 2002) during 1998–2002, separately. These are the entire interval over which each product is available.

During February the MLD and D_C are typically between 20 and 35 m and comparable to each other in the interior of the region (Figs. 5a,b). In contrast, the summer MLD is very shallow ($\approx$3 m) in most of the region and always shallower than D_C (Figs. 5c,d). Previously,
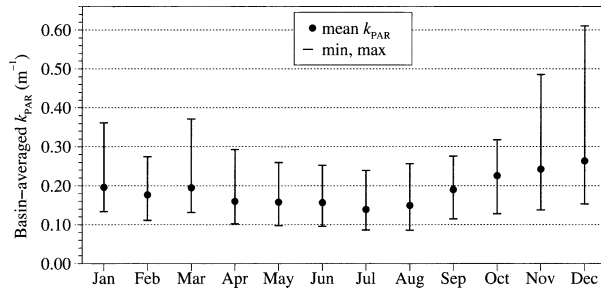
FIG. 3. Basin-averaged monthly mean k_{PAR} (m^{-1}) values for the fields shown in Fig. 2. Also shown is range (minimum and maximum) of k_{PAR} for each month. The smallest basin-averaged k_{PAR} value is 0.14 m^{-1} in Jun, and the largest is 0.26 m^{-1} in Dec.

FIG. 4. Climatological annual cycle of k_{PAR} (m^{-1}) at five different locations in the Black Sea: near the Bosporus in the southwestern Black Sea (41.4°N, 29.1°E); the northwestern shelf (45.5°N, 31.0°E); in the interior (43.0°N, 34.0°E); the northeastern Black Sea (44.0°N, 37.0°E); and near the northeastern Black Sea coast (41.2°N, 40.0°E). Attenuation depth (i.e., k_{PAR}^{-1}) is calculated using the SeaWiFS-based attenuation coefficients (i.e., k_{PAR}) values.

Oguz et al. (2000) reported a maximum value of 50 m for the light absorption depth, which is roughly consistent with the definition of D_C as used in this paper. The spatial distribution of D_C values based on the satellite data reveals that light absorption depths as large as 50 m are only evident around the Turkish coast and in the easternmost Black Sea as evident in both February and June (Figs. 5b,d).

In particular, the Black Sea has a very shallow summer MLD in comparison to much of the global ocean (e.g., Kara et al. 2003a). Because the MLD is very shallow and k_{PAR} values are generally very large in the Black Sea, upper-ocean quantities from an OGCM simulation should show significant differences based on the amount of solar radiation in summer. Shortwave radiation from ECMWF and NOGAPS varies greatly over the Black Sea in February and June (Figs. 5e–h). Shortwave radiation from NOGAPS is always larger than from ECMWF, and this is true for all months as evident from basin-averaged mean values (see Table 1). Typically, the NOGAPS shortwave radiation values are ≈25 W m^{-2} greater than ECMWF values throughout the seasonal cycle. The differences are due mostly to differences in cloudiness and the time periods used to create climatologies from the two products.

3. Model description

HYCOM contains a total of five prognostic equations: two for the horizontal velocity components, a mass continuity or layer thickness tendency equation, and two conservation equations for a pair of thermodynamic variables, such as salt and temperature or salt and density. The model behaves like a conventional σ (terrain following) model in shallow, unstratified oceanic regions, like a z-level coordinate model in the mixed layer or other unstratified regions, and like an isopycnic-coordinate model in stratified regions. Details of the HYCOM numerics are given in Bleck (2002). The vertical coordinate evaluation for HYCOM is discussed in Chassignet et al. (2003), and the mixed layer/vertical mixing options in HYCOM are evaluated in Halliwell (2004). In this paper, the major focus is the variation of upper-
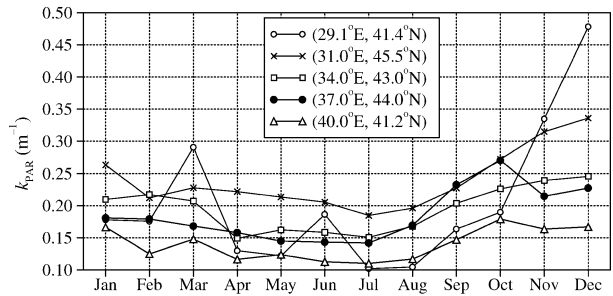
ocean quantities in the Black Sea. Thus, we only provide a brief description of the KPP mixed layer model and parameterization of quantities relevant to this study.

The KPP was the first nonslab mixed layer model (Large et al. 1997) included in HYCOM. It provides mixing from surface to bottom, smoothly matching the large surface boundary layer diffusivity/viscosity profiles to the weak diapycnal diffusivity/viscosity profiles of the interior ocean. There are numerous advantages to this model. In the ocean interior, the contribution of background internal wave breaking, shear instability mixing, and double diffusion (both salt fingering and diffusive instability) are parameterized. In the surface boundary layer, the influences of wind-driven mixing, surface buoyancy fluxes, and convective instability are parameterized. The KPP algorithm also parameterizes the influence of nonlocal mixing of temperature and salinity, which permits the development of countergradient fluxes.

The KPP model is semi-implicit, requiring multiple iterations. For the first iteration, vertical profiles of diffusivity/viscosity coefficients are calculated at model interfaces from the initial profiles of model variables. The model variables are then mixed by solving the one-dimensional vertical diffusion equation at each grid point. For the second iteration, the vertically mixed profiles of model variables are used to estimate new diffusivity/viscosity profiles, which are then used to mix the original profiles of model variables. This procedure should be repeated until the mixed profiles of model variables differ insignificantly from the mixed profiles obtained from the previous iteration. Given the computational overhead required for each iteration, the HYCOM tests revealed that two iterations are reasonably adequate. The KPP algorithm does not require a convection algorithm that mixes adjacent layers when the upper layer is denser than the lower layer because in such cases shear instability mixing will be large.

The full KPP procedure is first applied at pressure grid points, where thermodynamical variables and trac-
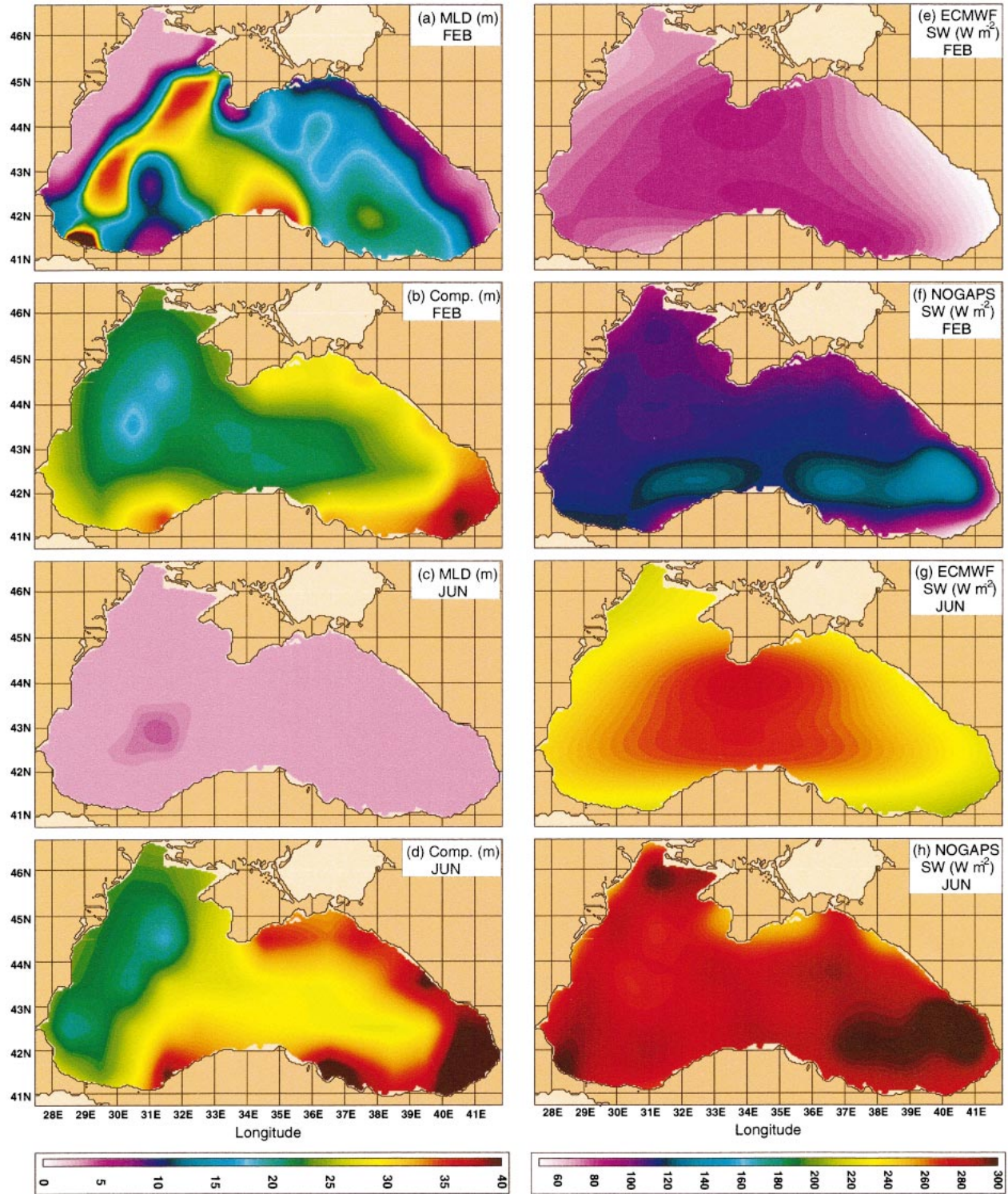
FIG. 5. Climatological mean of various quantities over the Black Sea: (a) Ocean MLD in Feb; (b) max PAR absorption depth D_C in Feb; (c) MLD in Jun; (d) D_C in Jun; (e) and (f) shortwave radiation from ECMWF and NOGAPS, respectively, in Feb; and (g) and (h) shortwave radiation from ECMWF and NOGAPS, respectively, in Jun.

Table 1. Basin-averaged climatological monthly mean values for MLD, D_C calculated using k_{PAR} values from SeaWiFS, and shortwave radiation from both ECMWF and NOGAPS. Also given are differences in shortwave radiation fluxes between NOGAPS and ECMWF (i.e., NOGAPS − ECMWF), and between maximum PAR absorption depth and mixed layer depth (i.e., D_C − MLD) as well. The MLD climatology for the Black Sea was constructed using temperature and salinity profiles from the 1/8° Generalized Digital Enviromental Model (GDEM) version 3 climatology (M. Carnes 2003, personal communication), which has 70 levels in the vertical. In the MLD criterion we calculate the density using the standard United Nations Educational, Scientific, and Cultural Organization (UNESCO) equation of state with no pressure dependence, that is, zero pressure (Millero et al. 1980; Millero and Poisson 1981).

	GDEM MLD (m)	SeaWIFS D_C (m)	Diff (m)	ECMWF SW rad* (W m⁻²)	NOGAPS SW rad* (W m⁻²)	Diff (W m⁻²)
Jan	20.4	24.1	3.7	38.8	62.8	24.0
Feb	17.0	26.7	9.7	70.2	94.0	23.8
Mar	11.1	24.7	13.6	123.7	147.4	23.7
Apr	4.6	29.7	25.1	176.2	208.0	31.8
May	3.2	30.0	26.8	218.6	246.6	28.0
Jun	3.0	30.5	27.5	236.3	265.7	29.4
Jul	3.3	34.1	30.8	227.8	264.9	37.1
Aug	4.6	31.9	27.3	199.4	230.0	30.6
Sep	6.1	24.9	18.8	149.1	176.4	27.3
Oct	9.7	21.0	11.3	92.6	121.7	29.1
Nov	13.1	20.0	6.9	48.9	78.0	29.1
Dec	14.8	18.8	4.0	32.5	54.3	21.8

*rad = radiation

ers are mixed. HYCOM is on a C-grid so momentum components are first horizontally interpolated to the pressure grid points. After completing the iterative procedure at pressure points, mixing is performed at momentum (u and v) points by interpolating the final viscosity profiles at the pressure points to the momentum points, then solving the vertical diffusion equation. The full iterative procedure is therefore not required at the momentum points.

a. Mixed layer depth

In the model, the turbulent surface boundary layer is calculated as part of KPP, while the MLD is a diagnostic quantity calculated as the first depth at which the density jump with respect to the surface is the equivalent of 0.2°C. The boundary layer thickness in the KPP model is usually close to MLD since vertical mixing is strong in the boundary layer.

Diagnosis of boundary layer thickness (h_b) in HYCOM is based on the bulk Richardson number:

$$\text{Ri}_b = \frac{[B_r - B(z)]d}{[\mathbf{v}_r - \mathbf{v}(z)]^2 + V_t^2(z)}, \quad (1)$$

$$B(z) = g[\alpha(T_s, S_s) - \beta(T_s, S_s)], \quad (2)$$

$$V_t^2(z) = \frac{C_v(-\beta_T)^{1/2}}{\text{Ri}_c \kappa^2}(c_s\varepsilon)^{-1/2}dNw_s, \quad (3)$$

$$N = \left(\frac{g}{\rho_o}\frac{\partial\rho}{\partial z}\right)^{1/2}, \quad (4)$$

$$\alpha(T_s, S_s) = \frac{-\partial\rho/\partial T}{\rho_o}, \quad (5)$$

$$\beta(T_s, S_s) = \frac{\partial\rho/\partial S}{\rho_o}. \quad (6)$$

The reader is referred to the appendix for a brief description of each symbol used in the formulations throughout the paper. In (1) the subscript r denotes reference values, and the two terms in the denominator represent the influence of resolved vertical shear and unresolved turbulent velocity shear, respectively. Reference values are averaged over the depth range εd, where $\varepsilon = 0.1$. At depth $d = h_b$, the reference depth εh_b represents the thickness of the surface layer where Monin–Obukhov similarity theory applies. In practice, if the first model layer is more than 7.5-m thick, reference values in (1) are set to the layer 1 value. Otherwise (e.g., in the Black Sea, with a 3-m top layer), averaging is performed over depth range εd. Note that the expansion coefficients for temperature and salinity in (2) are denoted as $\alpha(T, S)$ and $\beta(T, S)$, respectively.

The scalar turbulent velocity scale, w_s, in (3) is estimated as follows:

$$w_s = \kappa(a_s u_*^3 + c_s\kappa\sigma w_*^3)^{1/3} \rightarrow \kappa(c_s\kappa\sigma)^{1/3}w_*$$
$$\text{for } \sigma < \varepsilon, \quad (7)$$
$$w_s = \kappa(a_s u_*^3 + c_s\kappa\varepsilon w_*^3)^{1/3} \rightarrow \kappa(c_s\kappa\varepsilon)^{1/3}w_*$$
$$\text{for } \varepsilon \leq \sigma < 1, \quad (8)$$

where a_s and c_s are constants, $w_* = (-B_f h)^{1/3}$ is the convective velocity scale with B_f being the surface buoyancy flux, and $\sigma = d/h_b$. Expressions to the right of the arrows represent the convective limit. In HYCOM, w_s values are stored in a two-dimensional lookup table as functions of u_*^3 and σw_*^3 to reduce calculations.

The surface boundary layer thickness is the depth range over which turbulent boundary layer eddies can penetrate before becoming stable relative to the local buoyancy and velocity. It is estimated as the minimum depth at which Ri_b exceeds the critical Richardson number of $\text{Ri}_c = 0.3$. Moving downward from the surface,

Ri_b is calculated for each layer. When the first layer is reached where $Ri_b > 0.3$, h_b is estimated by linear interpolation at Ri_b between the central depths of that layer and the layer above.

If the surface forcing is stabilizing, the diagnosed value of h_b is required to be smaller than both the Ekman length scale (h_e^*) and the Monin–Obukhov length scale (L). In this case, we introduce a stable depth (h^*). The stable depth parameterization used in HYCOM is adopted from a layered ocean model embedded with a mixed layer submodel (Wallcraft et al. 2003; Kara et al. 2003b) as follows:

$$h^* = \min(L, h_e^*), \tag{9}$$

$$L = u_*^3/(0.4B_f), \tag{10}$$

$$h_e^* = 0.7u_*/\hat{f}, \tag{11}$$

$$u_*^2 = \tau_a/\rho_0, \tag{12}$$

$$B_f = -\frac{g\alpha(T_s, S_s)Q_a}{\rho_o C_w} + g\beta(T_s, S_s)(E - P)S_s, \tag{13}$$

$$f = 2\Omega \sin\phi, \tag{14}$$

$$\hat{f} = \max(|f|, f^+), \tag{15}$$

where the surface buoyancy forcing (B_f) includes contributions from both heat flux (Q_a) and salinity flux ($E - P$). Positive (negative) buoyancy flux indicates a buoyancy loss (gain).

b. Sea surface height

The sea surface height (SSH) in HYCOM is a diagnostic quantity described as follows:

$$\text{SSH} = \frac{1}{g}(M + \alpha_{\text{pref}}p), \tag{16}$$

$$M = p\alpha_p + gz, \tag{17}$$

$$\alpha_p = \frac{1}{\rho_0}, \tag{18}$$

where M is the Montgomery potential, α_{pref} is a reference value of specific volume taken as 10^{-3} m^3 kg^{-1}, and p is barotropic pressure. The Montgomery potential (M) is also a diagnostic model field, based on density and layer thickness, that appears on the right-hand side of the momentum conservation equation (as a pressure gradient or Montgomery potential gradient) as follows:

$$\frac{\partial \mathbf{u}}{\partial t} + \nabla\frac{\mathbf{u}^2}{2} + (\zeta + f)\mathbf{k} \times \mathbf{u} = -\nabla M - g\frac{\partial \tau_a}{\partial p}, \tag{19}$$

$$\zeta = \frac{\partial v}{\partial x_s} - \frac{\partial u}{\partial y_s}, \tag{20}$$

$$\nabla = \frac{\partial}{\partial x}\mathbf{i} + \frac{\partial}{\partial y}\mathbf{j}. \tag{21}$$

In the momentum conservation equation the effects of the atmospheric pressure gradient are neglected. The relative vorticity (ζ) is written in (x, y, s) coordinates, where s is a generalized vertical coordinate. Subscript, s, in (20) shows it is held constant during partial differentiation. Distances in x, y direction, as well as their time derivatives, u and v, respectively, are measured in the projection onto a horizontal plane.

c. Surface energy balance

Prior to executing the KPP algorithm, surface fluxes of thermodynamical variables and momentum are distributed entirely over the uppermost model layer, with the exception of penetrating shortwave radiation. Previously, the two-component (red and blue light) exponential decay model of Jerlov (1976) was used to calculate penetrating shortwave radiation in the original HYCOM code (Halliwell 2004). The depth of penetration was a function of water clarity represented by the Jerlov water type. The water type was assigned integer values from 1 through 5, with 1 representing the clearest water; however, the same value is used at all grid points for all time. This does not work in the Black Sea because the remotely sensed attenuation depths (see section 2) clearly revealed that attenuation of k_{PAR} can be highly variable over the Black Sea. With the new solar radiation penetration scheme (Kara et al. 2005a; Kara et al. 2005b), shortwave radiation can penetrate to deeper layers, with the penetration depth depending on water clarity as determined from the spatial and temporal varying attenuation depths from the Sea-WiFS data.

4. Black Sea model

The Black Sea model setup is introduced in Kara et al. 2005a in detail. Therefore, only a brief summary is provided here. The hybrid coordinate approach is accomplished using a hybrid-generator. The original remapper in HYCOM assumed that each field was constant in the vertical within each layer (Bleck 2002). When remapping layers that are far from isopycnal this approach can lead to excessive diffusion. The current remapper, as used in this paper, allows the profile to vary linearly across a layer if the layer is not close to being isopycnal, which significantly reduces diffusion.

a. General features

The model has a $\frac{1}{25}° \times \frac{1}{25}°$ cos(lat), (latitude × longitude) square mercator grid. Average grid resolution is 3.2 km in the Black Sea, ranging from a minimum of 3.05 km to a maximum of 3.37 km based on the square Mercator grid with $\frac{1}{25}°$ resolution on the equator. There are 15 hybrid layers in the vertical, and the target density (σ_t) values corresponding to layers 1 through 15 are 6.00, 9.00, 10.00, 11.00, 12.00, 12.80, 13.55, 14.30, 15.05, 16.20, 16.80, 16.95, 17.05, 17.15, and 17.20,

respectively. The top target densities are chosen to create fixed depth layers near the surface. The bottom topography (Fig. 1) is derived from the 1-min subregion of the Naval Oceanographic Office's (NAVOCEANO) Digital Bathymetric Data Base-Variable resolution (DBDB-V) data.

In the Black Sea model, the climatology is used only for initialization and surface salinity relaxation. The model is initialized using the temperature and salinity profiles from the Modular Ocean Data Assimilation System (MODAS; Fox et al. 2002). These climatological temperature and salinity fields are formed using a bimonthly temporal interval (Fig. 6).

b. Atmospheric forcing

The model reads in the following time-varying atmospheric forcing fields: wind stress, wind speed, and thermal forcing (air temperature, air mixing ratio, shortwave radiation, and net solar radiation). In this paper, the HYCOM simulations use wind/thermal forcing based on two different archived weather center products: 1) ECMWF Re-Analysis (ERA) monthly climatology (formed over 1979–93) at a grid resolution of $1.125° \times 1.125°$, and 2) operational NOGAPS monthly climatology (formed over 1998–2002) at a grid resolution of $1° \times 1°$.

All model simulations are performed using climatological monthly mean forcing fields interpolated to daily values. However, a high-frequency component (6 h) is added to the climatological wind forcing (Kara et al. 2005a). The net surface heat flux in the model includes effects of turbidity through the model monthly k_{PAR} fields based on SeaWiFS (see section 2). Latent and sensible heat fluxes at the air–sea interface are calculated based on model SST using efficient and computationally inexpensive bulk formulas that include the effects of dynamic stability (Kara et al. 2002) at each model time step. Shortwave and longwave radiation are obtained from ECMWF or NOGAPS. A longwave radiation correction is used in the simulations as described in Kara et al. (2005b) in detail.

The model treats rivers as a runoff addition to the surface precipitation field. The flow is first applied to a single ocean grid point and then smoothed over surrounding ocean grid points, yielding a contribution to precipitation in m s^{-1}. In the Black Sea model, there are six major rivers, and we have compared monthly mean river discharge values obtained from various sources (Fig. 7). A brief explanation for each dataset is given here. The River Discharge (RivDIS) dataset (Vörösmarty et al. 1997) contains monthly discharge measurements. The monthly mean discharge in m^3 s^{-1} was derived by summing all available discharge measurements for a particular month and dividing by the number of measurements. The University Corporation for Atmospheric Research (UCAR) database contains real-time monthly averaged river discharges. A problem with

this dataset is that the measurements are often some distance from the mouth of the river. The NRL river database mainly comes from the RivDIS and Perry et al. (1996) datasets. The latter had one mean value for each river but the set was converted to monthly values to be used in real-time ocean modeling studies at NRL. The annual mean flow values reported by Perry et al. (1996) were compiled from different sources published in the literature (e.g., Milliman and Meade 1983; Kempe et al. 1991; Meybeck 1988; Dynesius and Nilsson 1994). Based on a statistical analysis (not shown) it was found that there is a good agreement between RivDIS and other datasets. The RivDIS dataset is used here because it gives river discharge values at the mouth of the river.

c. Model simulations

The climatologically forced model simulations use three different k_{PAR} values. For experiment 1, spatially and monthly varying k_{PAR} values interpolated to the HYCOM grid are used. In experiment 2, all of the solar radiation is absorbed in the mixed layer by using a very large k_{PAR} value of 99.9 m^{-1}. For experiment 3, the water turbidity over the Black Sea is set to a constant, $k_{PAR} = 0.06$ m^{-1}, which is a representative value for clear water (e.g., Kara et al. 2004). Simulation experiments 1, 2, and 3 use wind/thermal forcing from ECMWF, while experiments 4, 5, and 6 are essentially twins of experiments 1, 2, and 3 but use wind/thermal forcing from NOGAPS.

The clear water assumption is used to assess the impact of turbidity in the Black Sea simulations. It also demonstrates the consequences if the Black Sea model were included as part of a global model which assumes clear water everywhere. Using two different atmospheric products in forcing the model simulations helps us assess the sensitivity to choice of atmospheric forcing product and the relative impact and type of impact due to turbidity and differences between forcing products. In experiments 3 and 6, the e-folding penetration depth of k_{PAR}^{-1} is 16.7 m with 95% absorption by 50-m depth. Experiments 2 and 5, which assume all radiation absorbed at the sea surface, represent the traditional OGCM approach (e.g., Yuen et al. 1992).

5. Water turbidity effects on upper-ocean quantities

Using the model simulations introduced in section 4c, we first investigate water turbidity effects on the seasonal variability of the basinwide mean heat flux and mixed layer flux over the Black Sea (Fig. 8). The mixed layer flux is the heat flux absorbed in the mixed layer in the model simulations. The difference between the two is the shortwave radiation absorbed below the mixed layer. Since experiment 2 (ECMWF wind/thermal forcing) and experiment 5 (NOGAPS wind/thermal forcing) assume all radiation absorbed at the sea surface, bas-
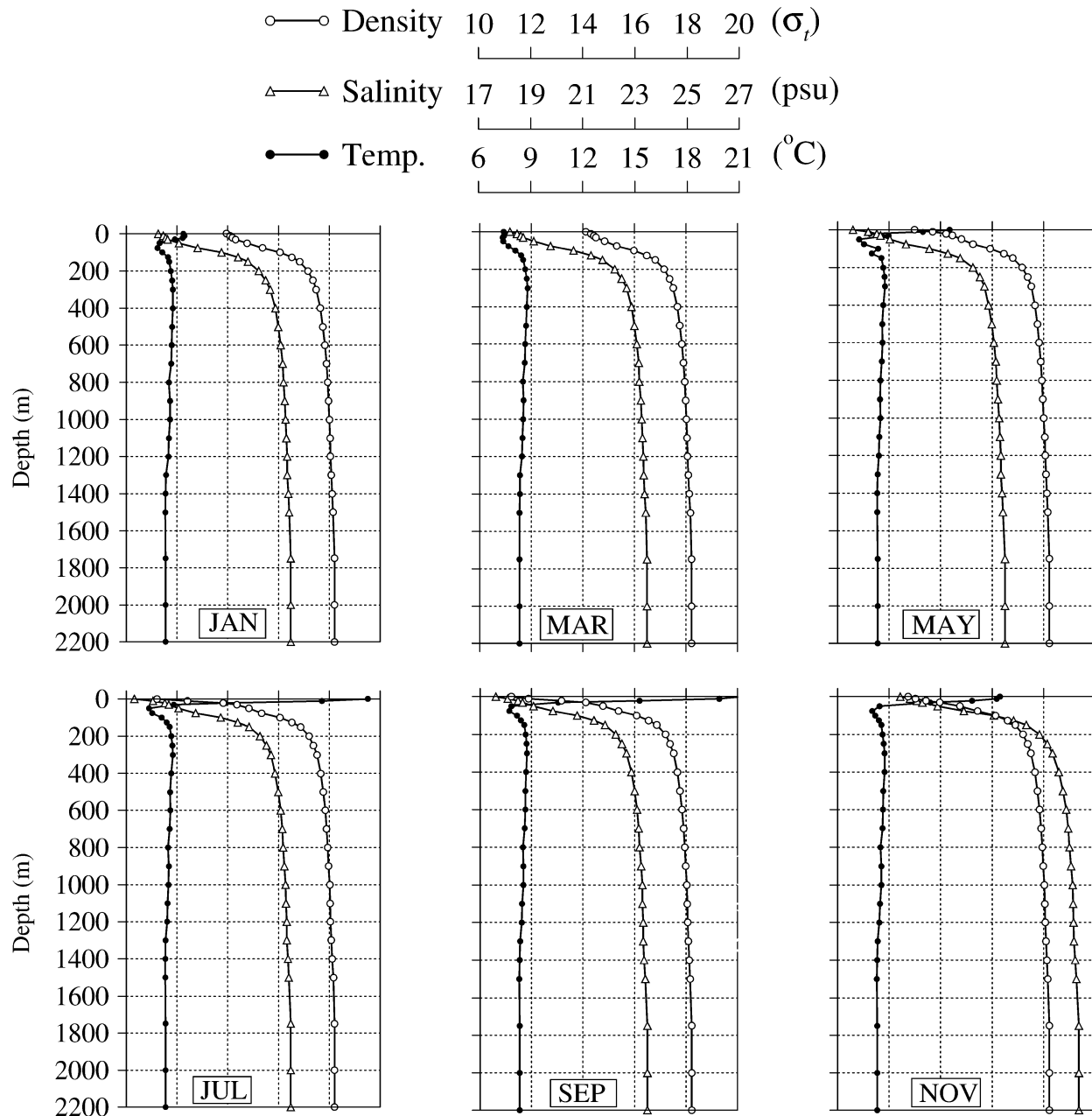
FIG. 6. Basin-averaged bimonthly potential temperature, salinity, and potential density profiles obtained from the MODAS climatology used in the model initialization. Climatology for the Black Sea model is output at 27 depth levels ranging from 0 to 2200 m. As explained in Kara et al. (2005a), a simple linear extrapolation was applied to the temperature and salinity profiles, so that they could be extended below 1750 m because the MODAS climatology does not have any profile below that depth. This linear extrapolation is reasonable given the fact that temperature and salinity of the deep water masses do not change very much on the climatological time scales so they can be considered as quasi-steady.

inwide mean heat flux equals the mixed layer flux, so they are not shown.

As expected, the basinwide annual mean heat flux is zero for each simulation (see Fig. 8) because any closed domain must have zero net heat flux at equilibrium. The bulk heat flux approach converts any initial nonzero annual net heat flux adjustment into SST adjustments that tend to reduce the annual heat flux imbalance. Although basinwide mean heat flux is zero for each simulation, heat flux values throughout the year are different for each simulation because the model-calculated sensible and latent heat fluxes, which are based on model sea surface temperature, are different. There is usually heat loss from October through mid-March in all sim-
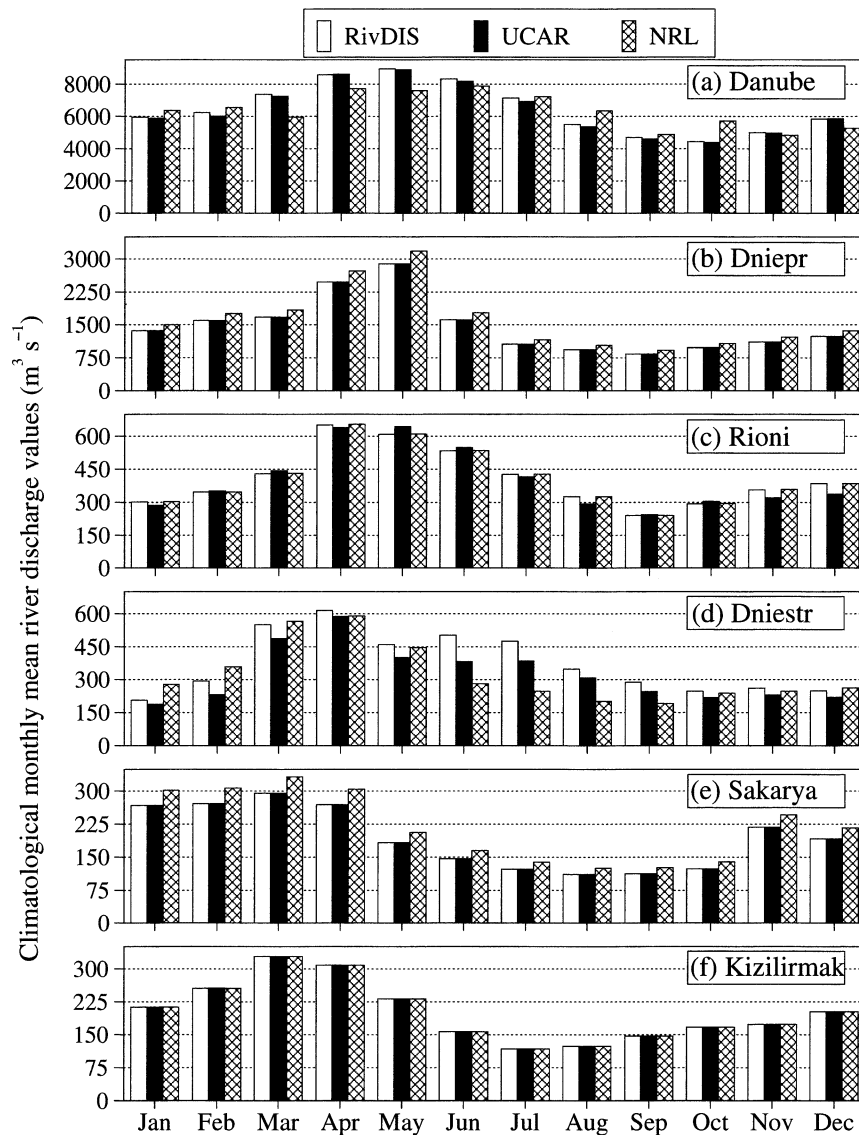
FIG. 7. Climatological monthly mean flow values (m³ s⁻¹) obtained from three datasets for the rivers used in the HYCOM Black Sea simulations: (a) Danube, (b) Dniepr, (c) Rioni, (d) Dniestr, (e) Sakarya, and (f) Kizilirmak. (a)–(f) Note that the *y*-axis scaling is different for each. Sources for these datasets and time periods during which climatological river discharges were constructed are given in Kara et al. (2005a). The NRL dataset is similar to RivDIS except for a scale factor to correct the annual mean.

ulations. The mixed layer flux is almost identical to the mean heat flux at the sea surface during this time period. On the contrary, there is usually a heat gain from mid-March through September, and the net heat flux reaches its maximum in summer, due mostly to the large short-wave radiation (see Figs. 5g,h). The mixed layer flux amplitude is clearly different when using spatially and temporally varying attenuation depths in experiment 1 in comparison to the clear water constant solar atten-uation depth case (experiment 3) both of which use the same ECMWF wind/thermal forcing. In the latter, there is less mixed layer flux in summer. Similarly, a com-

parison of experiments 4 and 6 reveals the same type of result.

Figure 9 shows basinwide mean differences between the net flux at the sea surface and the mixed layer flux calculated for each simulation. The difference is much larger in experiment 3 than experiment 1, similarly for experiment 6 versus experiment 4. Thus, the use of the constant clear water attenuation depth clearly results in greater solar penetration flux below the mixed layer than the simulations which use SeaWiFS-based spatially and temporally varying attenuation depths, regardless of which atmospheric forcing is used. Overall, the basin-
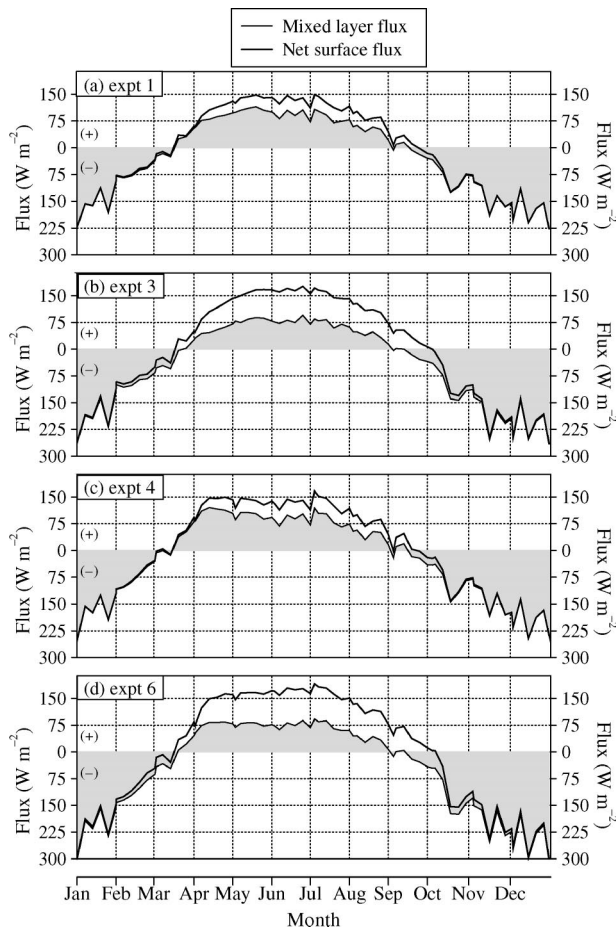
FIG. 8. Climatological Black Sea–wide mean heat flux and the portion absorbed in the mixed layer: (a) experiment 1, which uses ECMWF wind/thermal fluxes and k_{PAR} as processed from SeaWiFS ocean color data, (b) experiment 3, which uses ECMWF wind/thermal forcing and a clear water constant k_{PAR} value of 0.06 m^{-1}, (c) experiment 4, which uses NOGAPS wind/thermal fluxes and k_{PAR} from SeaWiFS, and (d) experiment 6, which uses ECMWF wind/thermal forcing and a clear water constant k_{PAR} value of 0.06 m^{-1}. (a)–(d) The difference between the two curves is the shortwave radiation absorbed below the mixed layer.

FIG. 9. Climatological Black Sea–wide mean shortwave radiation absorbed below the mixed layer for the simulations shown in Fig. 8: (a) experiments 1 and 3 when HYCOM was forced with ECMWF wind/thermal fluxes, and (b) experiments 4 and 6 when HYCOM was forced with ECMWF wind/thermal fluxes. The difference between the net heat flux and mixed layer flux for experiments 2 and 5 is zero because both simulations assume all radiation absorbed at the sea surface, so they are not shown. The basin-averaged annual mean differences are 17 and 41 m^{-2} for experiments 1 and 3, and they are 19 and 48 m^{-2} for experiments 4 and 6.

wide difference between the net heat flux at the sea surface and mixed layer flux can be as large as 50 W m^{-2} for experiments 1 and 4 (100 W m^{-2} for experiments 3 and 6) during summer months.

The impact of water turbidity on MLD predictions is shown in Fig. 10, demonstrating that the clear water constant solar attenuation depth assumption results in relatively deep MLDs in comparison to the standard simulations. As expected, the largest differences are seen in winter and early spring (Fig. 11) because MLD is usually deep during these seasons. Although MLD differences are relatively small from May to October, this does not mean that water turbidity has little effect on the model simulations. This can be explained in terms of a buoyancy flux [Eq. (13)], which assesses the influence of the atmosphere on the ocean. Changes in upper-
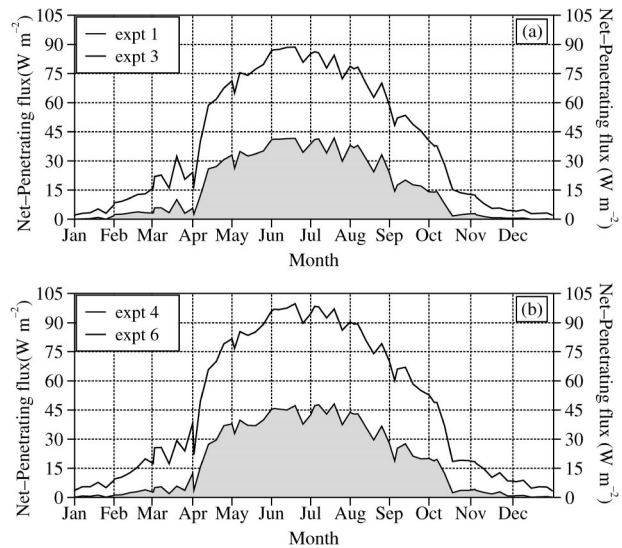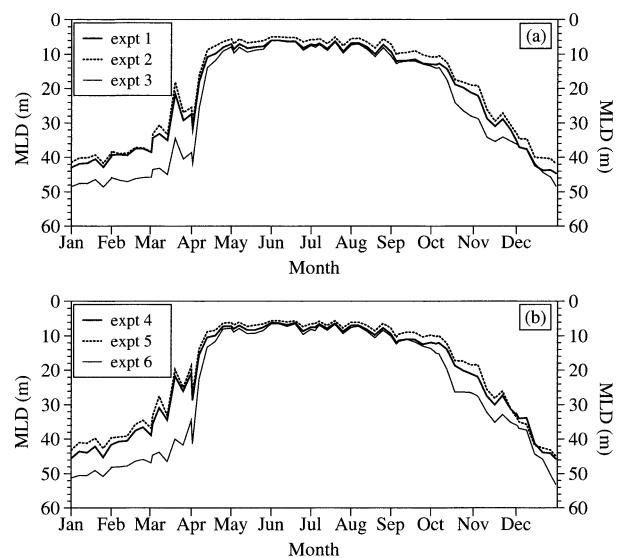

FIG. 10. Basin-averaged climatological mean MLD in the Black Sea: (a) experiments 1, 2, and 3 when HYCOM was run with ECMWF wind/thermal forcing, and (b) experiments 4, 5, and 6 when HYCOM was run with NOGAPS wind/thermal forcing. The climatological mean MLD was formed using model years 5–8. Basin-averaged annual mean MLD values are 18.3, 17.5, and 21.7 m for experiments 1, 2, and 3, respectively. Similarly, they are 18.0, 17.0, and 22.1 for experiments 4, 5, and 6, respectively. There are 6 days between model diagnostic values.
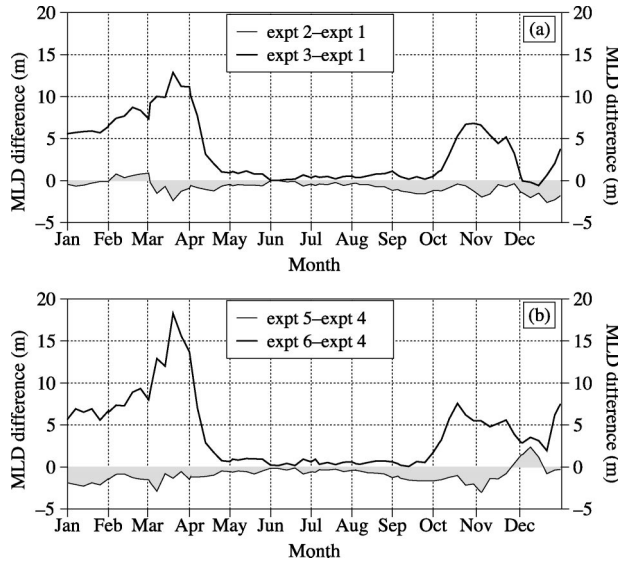
FIG. 11. Basin-averaged climatological mean MLD differences between the simulations shown in Fig. 10.

FIG. 12. The same as in Fig. 10 but for the buoyancy flux. Note that values on the y axis must be multiplied by 10^{-9} to obtain actual buoyancy flux values. There are 6 days between model diagnostic values.

ocean buoyancy occur when the temperature (salinity) changes due to fluxes of heat (freshwater). A buoyancy gain by the Black Sea is evident from March through September, revealing that the upper ocean stabilizes (Fig. 12) because this causes an increase in stratification. In contrast, the net buoyancy flux tends to destabilize the ocean surface layer in other months, especially in winter. While there are no significant differences in MLD between experiments 1 and 2 (or experiments 4 and 5) in summer, large differences exist in net buoyancy flux (Fig. 13), that is, differences due to absorbing all radiation at the sea surface versus using the monthly k_{PAR} climatology from SeaWiFS data. This is especially evident in summer. Differences in buoyancy flux magnitudes also result in changes in density. For example, buoyancy flux from experiment 1 (experiment 4) is significantly less than that from experiment 3 (experiment 6) during October and November, demonstrating that the density is reduced when using the clear water constant solar attenuation depth assumption. As expected, such changes in density affect stratification near the sea surface. Thus, the decrease in density due to the increase in the buoyancy flux is an obvious example of the impact of water turbidity on the upper-ocean stability.

The basin-averaged buoyancy flux [see Eq. (13)] is further analyzed in order to discuss the relative contributions of heat (thermal) and salt (haline) fluxes at the ocean surface. The ratio (R) of the thermal and haline flux components is given by $R = |\alpha(T_s,S_s)Q_a/\rho_o C_w \beta(T_s S_s)(E - P)S_s|$. Relatively large difference in the net surface buoyancy fluxes between experiments 1 and 2 (similarly, between experiments 4 and 5) is a clear effect of heat flux rather than freshwater flux because (a) buoyancy is much more sensitive to variations in heating, and (b) salinity flux is not very sensitive to the
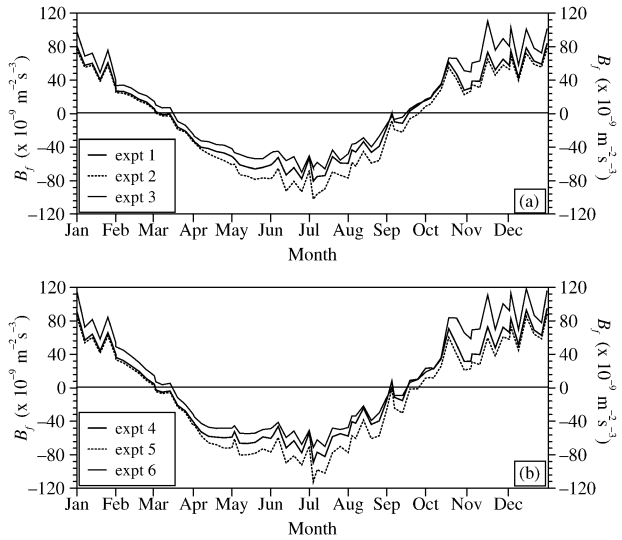
water turbidity (Table 2). The thermal buoyancy flux clearly dominates over the haline buoyancy flux in almost all months as evident from very large buoyancy ratio values ($R \gg 1$) in all months except March and April. The freshwater flux determines buoyancy in March ($R \ll 1$); however, the ratio becomes order of unity when using the clear water constant depth attenuation assumption (experiments 3 and 6), that is, heat and freshwater fluxes are of the same magnitude.

As an example, thermal and haline surface buoyancy fluxes from experiment 4 are shown along with the buoyancy ratio values (Fig. 14). It is noted that stratification is usually strong, and the buoyancy flux values
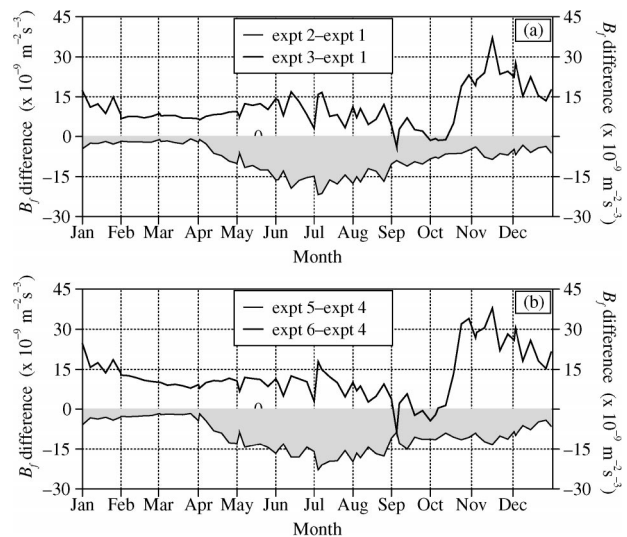

FIG. 13. Basin-averaged climatological mean buoyancy flux differences between the simulations shown in Fig. 12.

TABLE 2. Components of the basin-averaged monthly mean buoyancy flux in the Black Sea: surface buoyance due to net heat flux (thermal) and surface buoyancy due to net freshwater flux (haline). All values must be multiplied by 10^{-9}. Also given are buoyance ratio [$R = B_f$(thermal)/B_f(haline)] values, demonstrating the relative impact on upper-ocean buoyancy of heating and salinity effects, where $|R| \approx 1$ explains that the buoyancy appears to be equally affected by heating and salinity effects. Note that the lack of basin-averaged annual mean buoyancy flux balance is due to the fact that the conversion from heat to buoyancy depends on sea surface temperature and sea surface salinity varying significantly from winter to summer, and the basinwide average of buoyancy flux is a weighted sum of thermal and haline fluxes.

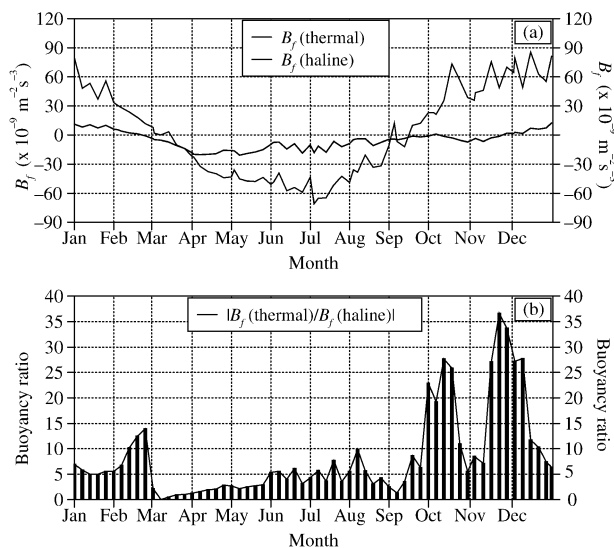| Month	Buoyancy flux (thermal)			Buoyancy flux (haline)			Buoyancy flux ratio (|R|)		
	Expt 1	Expt 2	Expt 3	Expt 1	Expt 2	Expt 3	Expt 1	Expt 2	Expt 3
Jan	47	44	61	12	12	10	3.9	3.7	6.1
Feb	19	16	27	5	4	3	3.8	4.0	9.0
Mar	1	−1	9	−8	−8	−9	0.1	0.1	1.0
Apr	−25	−31	−15	−18	−18	−20	1.4	1.7	0.8
May	−47	−60	−34	−14	−13	−15	3.4	4.6	2.3
Jun	−56	−74	−44	−13	−13	−14	4.3	5.7	3.1
Jul	−48	−65	−38	−10	−10	−11	4.8	6.5	3.5
Aug	−21	−34	−15	−5	−5	−6	4.2	6.8	2.5
Sep	8	−2	12	−1	−1	−3	8.0	2.0	4.0
Oct	39	33	51	−2	−2	−2	19.5	16.5	25.5
Nov	54	48	76	1	1	4	54.0	48.0	19.0
Dec	58	53	76	9	9	10	6.4	5.9	7.6
	Expt 4	Expt 5	Expt 6	Expt 4	Expt 5	Expt 6	Expt 4	Expt 5	Expt 6
Jan	47	52	74	9	9	10	5.2	5.8	7.4
Feb	19	21	36	3	3	3	6.3	7.0	12.0
Mar	1	−6	9	−9	−8	−9	0.1	0.8	1.0
Apr	−25	−43	−24	−18	−18	−19	1.3	2.4	1.2
May	−47	−61	−34	−15	−13	−15	3.1	4.7	2.3
Jun	−56	−75	−45	−13	−13	−14	4.3	5.8	3.2
Jul	−48	−68	−39	−10	−9	−10	4.8	7.6	3.9
Aug	−21	−30	−12	−6	−5	−8	3.5	6.0	1.5
Sep	8	−2	14	−2	−1	−5	4.0	2.0	2.8
Oct	39	33	62	−3	−4	−4	13.0	8.3	15.5
Nov	54	50	86	−2	−2	1	27.0	25.0	86.0
Dec	58	63	91	6	6	6	9.7	10.5	15.2

FIG. 14. The basin-averaged thermal and haline buoyancy fluxes from experiment 4 (wind/thermal forcing are from NOGAPS), which uses spatial and temporal varying attenuation depths. Buoyancy ratio [B_f(thermal)/B_f(haline)] values are also shown. There are 6 days between model diagnostic values.

are usually on the order of 10^{-8} in the Black Sea. Thus, the convection does not usually extend to greater depths when exposed to buoyancy loss of these magnitudes. As an example, Marshall and Schott (1999) explained that buoyancy forcing needs to be on the order of $>10^{-7}$ for convection to reach depth ≈ 2 km, which is not the case for the Black Sea.

The impact of water turbidity on surface currents is now examined during February and June. These two months are chosen primarily because (i) the difference between the net surface heat flux and mixed layer flux is very large in June (see Fig. 9), and (ii) the climatological MLD is deeper than the D_C in some regions (e.g., in the western Black Sea) in February, and the MLD is always shallower than the D_C in June as shown previously (see Fig. 5). All model results are presented based on monthly means that are constructed from the last 4 yr of the model simulations. At least a 4-yr mean is needed because nondeterministic flow instabilities are a major contribution to circulation features in HYCOM Black Sea simulations at 3.2-km resolution.

There are differences in the number and magnitude of the coastal eddies in the eastern part of the Black Sea in February among all simulations (Fig. 15a). This
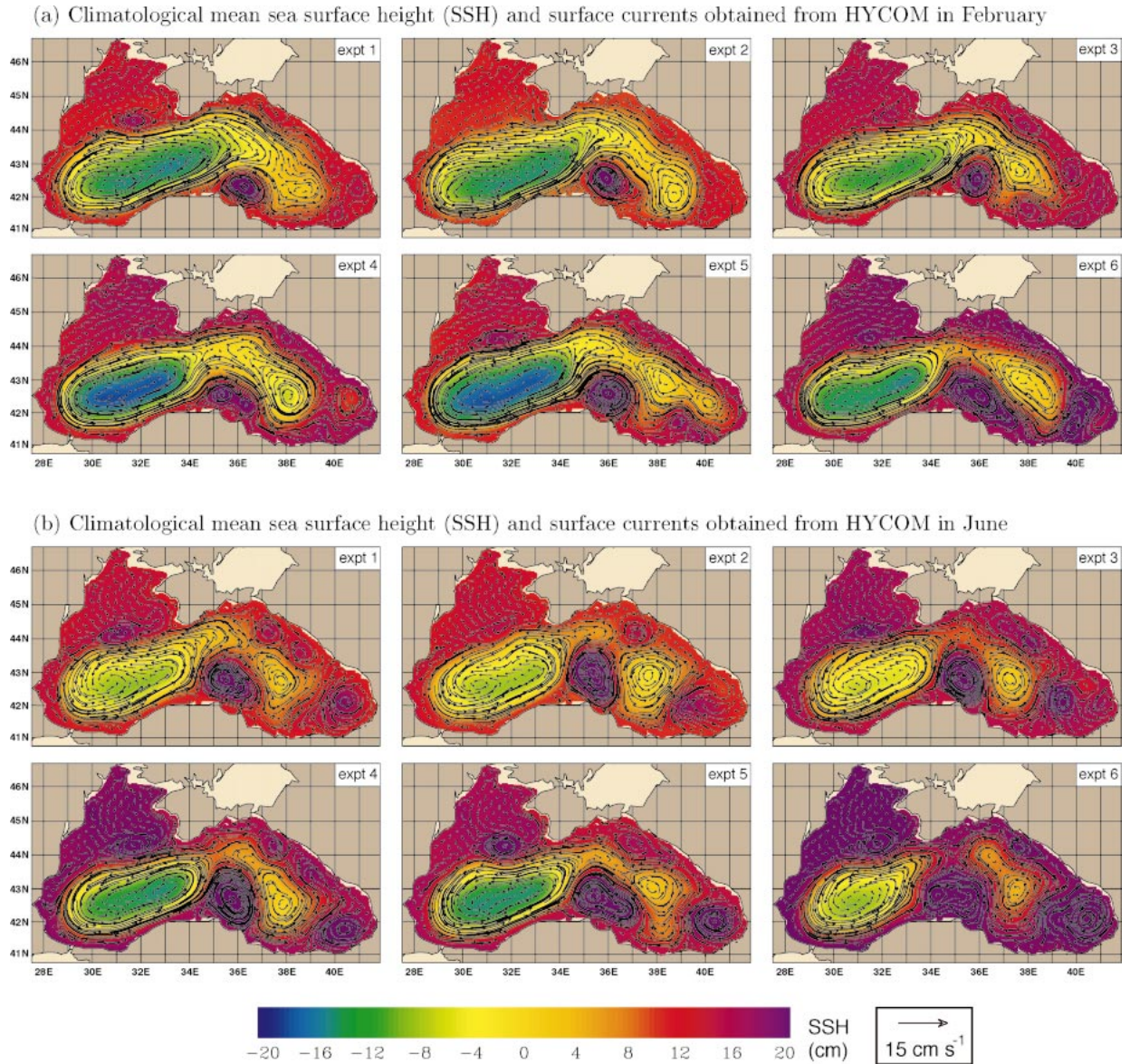
(a) Climatological mean sea surface height (SSH) and surface currents obtained from HYCOM in February

(b) Climatological mean sea surface height (SSH) and surface currents obtained from HYCOM in June

FIG. 15. Mean surface layer currents (cm s^{-1}) overlain on mean sea surface heights (cm) averaged over 4 yr (model yr 5–8) in the Black Sea: (a) Feb and (b) Jun. Simulation experiments 1, 2, and 3 were forced with ECMWF wind and thermal fluxes, and simulation experiments 4, 5, and 6 were forced with NOGAPS wind and thermal fluxes. The length of the reference velocity vector is 15 cm s^{-1}.

is especially evident when using spatially and temporally varying attenuation depths as opposed to clear water constant solar attenuation depths (i.e., experiment 1 versus experiment 3 and experiment 4 versus experiment 6). The use of a clear water constant solar attenuation depth results in more eddies. While there are no significant differences in the sea surface currents and SSH values when comparing standard cases to all radiation at the surface cases (i.e., experiments 2 and 5) on the annual time scales (see Kara et al. 2005a), it is clear that there are differences in February, and this is especially true for the simulations forced with NOGAPS wind and thermal fluxes. For example, the Sinop eddy

in experiment 4 is not as strong as the one in experiment 5, and there are two small eddies in experiment 4. The cyclonic western gyre with relatively large and negative SSH values is evident in both standard simulations. In the case of ECMWF versus NOGAPS wind/thermal forcing, SSH values in experiment 1 in the western gyre are smaller than those in experiment 4 by 10 cm. The anticyclonic Trabzon eddy in the easternmost Black Sea exists in experiment 1 in February but it is not seen in experiment 4, showing the impact of using different atmospheric forcing on the model simulations.

The effects of water turbidity on the upper-ocean circulation are easily seen in June (Fig. 15b) as the D_C is

much deeper than the MLD ($\approx$3 m) over the Black Sea, and shortwave radiation is very large (see Figs. 5g,h). The location and magnitude of the Sinop eddy remains the same regardless of the water turbidity when using ECMWF wind/thermal forcing (experiments 1, 2, and 3); while the same is not true for the NOGAPS wind/thermal forcing cases. Absorption of all radiation at the sea surface (experiment 5) and the use of clear water constant solar attenuation depth value of $\approx$17 m (experiment 6) yields a different current structure off Sinop. The anticyclonic Batumi eddy in the easternmost Black Sea is evident in experiments 1 and 4 with slightly different locations. In general, as in the winter case, the shallow northwestern part of the region has a limited number of eddies in comparison to other regions of the basin, although the anticyclonic Sevastopol eddy west–southwest of the Crimea Peninsula is seen in all of the simulations with varying strength. As indicated in Oguz and Besiktepe (1999), who examined hydrographic data, the Rim Current system, the cyclonic gyres of the interior, and a series of anticyclonic eddies around the periphery are fundamental features of the summer–autumn circulation in the Black Sea. The Rim Current usually flows cyclonically along the periphery of the basin, confined over the steepest topographic slope. These are evident in all of the HYCOM simulations.

6. Evaluation of seasonal HYCOM SSH variability

In this section, a monthly mean SSH anomaly climatology is introduced to validate SSH from HYCOM. The climatology is constructed using all available satellite altimeter data from the beginning of 1993 to the end of 2002 as obtained from analyses like the daily operational MODAS 2D SSH (Fox et al. 2002) except that these analyses are performed later when data centered about the analysis time and better altimeter orbits are available. Later, monthly mean SSH anomalies from HYCOM are compared with these newly developed climatological fields.

a. Monthly SSH anomaly climatology for the Black Sea

The climatology presented here is based on a merger of the TOPEX/Poseidon (T/P) satellite (January 1993–August 2002), the European Earth Remote-Sensing *ERS/ENVISAT* satellite (January 1995–onward) and the U.S. Navy *Geosat* Follow-On GFO satellite (December 2000–onward). The ground tracks of the three altimeters in the Black Sea and surrounding areas are shown in Fig. 16a. The repeat periods are approximately 10 days for T/P, 35 days for ERS, and 17 days for GFO. It should be noted that *Jason* tracks are the same as TOPEX/Poseidon. The satellite data used here are obtained from the altimeter products released by the operational real-time U.S. Navy system available online on the web (http://www.ocean.nrlssc.navy.mil/altimetry).

Altimetric deviations from their mean are obtained by using $SSH_{altimeter}$ = altimeter measurement $-$ $\langle$altimeter measurement$\rangle_{alt}$, where "$\langle\ \rangle_{alt}$" refers to an averaging over the altimeter data collection period from 1993 to 2002. This is done for T/P but the averages for the other two satellites over their more limited time interval are modified by referencing them to the T/P mean (e.g., Jacobs and Mitchell 1997). Daily SSH estimates start with an optimal interpolation of the altimeter datasets onto a ¼° $\times$ ¼° (latitude $\times$ longitude) grid in the Black Sea to develop a field of height deviation from the altimetric mean. The ground tracks show spatial gaps that are sometimes wide enough that mesoscale features may lie between them even when data from all three satellites are available. Thus, the space–time interpolation is not trivial for a given day. An optimal interpolation procedure used for obtaining daily SSH anomaly values is strongly dependent on the covariance function that is essential for calculating SSH anomalies at grid points that are far from the satellite ground tracks (Jacobs et al. 2001).

The monthly anomaly climatology is obtained after subtracting the annual mean from each month. The original daily SSH values are relative to an altimeter mean (i.e., anomaly with respect to the altimeter mean at each grid point). Using these daily values, we first formed a monthly and an annual mean SSH climatology. We then subtracted the annual mean from the February and June SSH climatologies (i.e., anomaly with respect to the annual mean at each grid point) to obtain monthly climatologies shown in Fig. 16b.

The February SSH anomaly climatology for the Black Sea is dominated by negative anomalies, ranging from -5.7 to 0.3 cm. Negative anomalies are typical of the winter months, while SSH anomalies are positive over most of the Black Sea in summer. The SSH anomaly also has a large range in summer, with the largest being in June when the SSH anomaly ranges from -0.2 to 11.9 cm. Negative SSH anomalies again dominate the Black Sea after summer (e.g., in October). The cycle of predominantly positive and negative anomalies represents the steric signal due to seasonal heating and cooling in the climatology. The regions of the highest sea level variability usually overlay the locations of the quasi-permanant features such as the anticyclonic Batumi eddy located in the easternmost part of the Black Sea, and the anticyclonic Sevastopol eddy centered at around 44°N, 31°E, both in June. These features are also evident in the standard HYCOM simulations (see Figs. 15a and 15b). Overall, the reader is cautioned that the climatology is smooth because the optimal interpolation was performed on a ¼° $\times$ ¼° grid using length scales of 60–100 km in the Black Sea.

Figure 17 shows daily time series (1993–2002) used in constructing the monthly anomaly climatology at various locations. These generally show the robust cycle with positive anomalies in summer and negative in the

(a) Satellite altimeter repeating ground tracks of the three altimeters around the Black Sea from 1993 to 2003
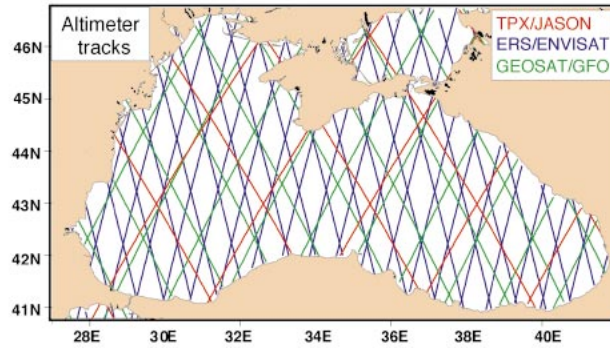
(b) SSH anomaly (cm) climatology processed from the post–operational U.S. Navy MODAS 2D altimeter data set
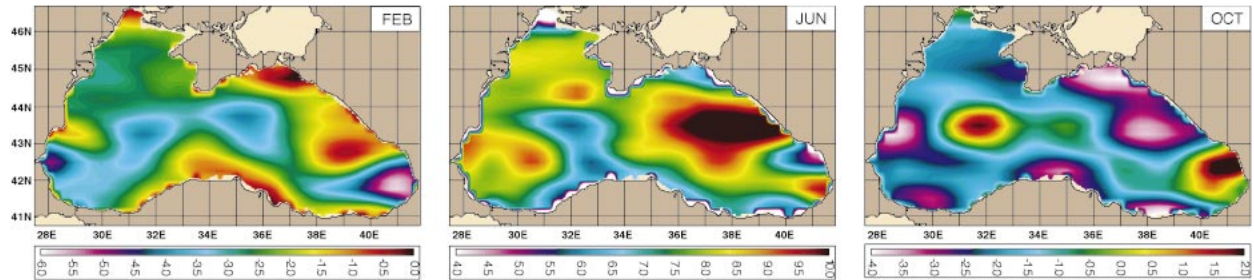
(c) RMS difference values (cm) between monthly mean HYCOM SSH anomalies and MODAS 2D SSH anomalies
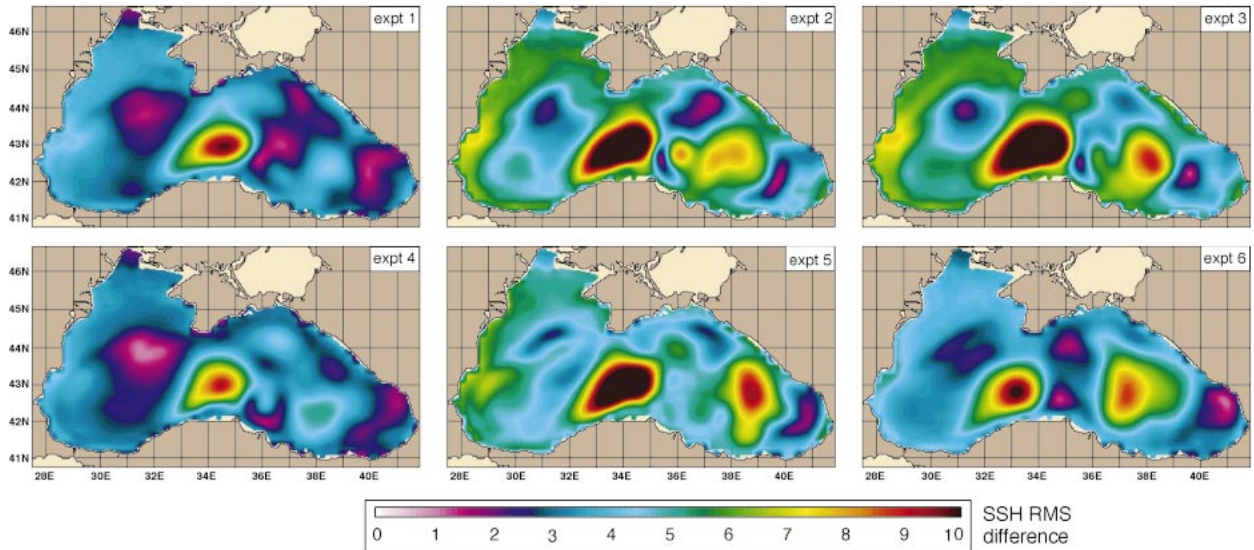

FIG. 16. (a) Altimeter repeating ground tracks around the Black Sea from 1993 to 2003: T/P and *Jason-1* (red), *ERS/ENVISAT* (blue), and *Geosat/GFO* (green). (b) SSH anomaly climatologies in Feb, Jun, and Oct. (c) Rms difference values between monthly mean HYCOM SSH anomalies and monthly mean SSH anomalies from analyses of satellite altimeter data during 1993–2002. For the model–data comparisons, we first calculated monthly mean SSH values using daily postoperational MODAS 2D altimeter SSH anomalies relative to a 10-yr mean during 1993–2002. We then substracted the annual mean of these new fields from each month to obtain a monthly mean SSH anomaly climatology. It is noted that in ''SSH anomaly,'' anomaly refers to the deviation from the altimetric mean SSH signal averaged over the altimeter measurement period of 1993–2002, while in ''monthly mean SSH anomaly climatology,'' anomaly refers to the difference from the annual mean of daily analyses of altimeter height anomalies.
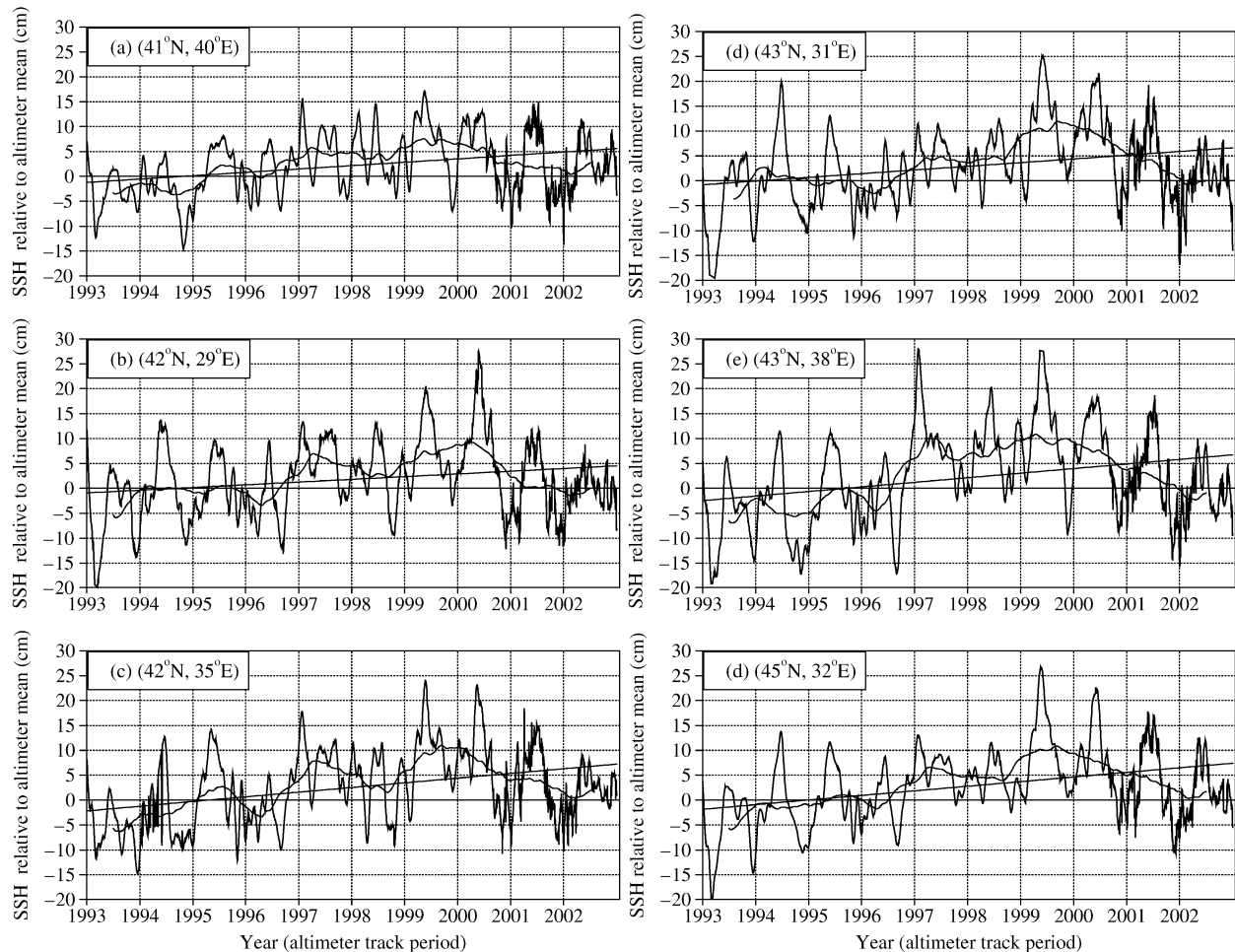
FIG. 17. Daily SSH anomaly values obtained from optimal interpolation of the altimeter datasets at various locations in the Black Sea. Also included are least squares lines and 1-yr running averages. Note that the *x* axis is labeled starting from the beginning of each year.

winter. There is a positive trend in sea level at locations in the interior of the Black Sea.

b. Model–data comparisons

Model–data comparisons are made to measure the performance of HYCOM in predicting climatological SSH anomaly over the seasonal cycle. This is done for each model simulation separately because our purpose is to determine sensitivity of HYCOM SSH prediction to water turbidity.

Before performing any model–data comparisons, the SSH anomaly climatology which originally had a grid resolution of $\frac{1}{4}° \times \frac{1}{4}°$ was interpolated to the model grid, and the trend was removed. HYCOM is quasi mass conserving, so its basinwide mean SSH is not constant. This allows a basin-averaged seasonal steric signal. Thus, the climatology presented in section 6a is roughly consistent with HYCOM. The monthly means were constructed using daily HYCOM SSH fields over the last 4 yr (model years 5–8) of the climatologically forced

simulation and the daily altimetric SSH analyses over 1993–2002. In both cases, the annual mean was subtracted from the monthly mean, and the differences were calculated using the $\frac{1}{4}°$ altimetric analyses interpolated to the model grid.

The root-mean-square (rms) difference between monthly mean SSH values from the climatologically forced HYCOM simulations and those from the altimetric climatology described in section 6a is calculated at each model grid point over the Black Sea (Fig. 16c). Overall, the rms differences are smaller for the standard simulations (i.e., experiments 1 and 4) that use Sea-WiFS-based space–time-varying attenuation depths in comparison to the other simulations. In particular, the basin-averaged rms differences are 3.9, 5.4, and 5.7 cm for experiments 1, 2 and 3. Similarly, they are 3.7, 5.3, and 5.9 cm for experiments 4, 5, and 6, respectively. Simulations that use clear water constant solar attenuation depths (i.e., experiments 4 and 6) result in the worst SSH predictions. In comparison to the standard simulations, it is also clear that absorbing all radiation

at the sea surface (i.e., experiments 2 and 5) yields a relatively large rms difference, and this is true when using both ECMWF wind/thermal forcing and NOGAPS wind/thermal forcing.

The model success in predicting SSH is especially evident from the standard simulations in the easternmost Black Sea where the Batumi and Trabzon eddies are usually present. The rms differences are as small as 1 cm in this region. In general, the use of atmospheric forcing from NOGAPS rather than ECMWF yields the best SSH simulations by HYCOM, although the differences between the two are small if one compares basin-averaged rms differences (3.9 cm for experiment 1 versus 3.7 cm for experiment 4).

Previously, monthly mean SST from HYCOM was compared to the $\frac{1}{8}°$ Pathfinder SST climatology, and it was found that SST rms differences were not large when using the monthly varying attenuation depths as opposed to the simulation which assumes all radiation absorbed at the sea surface (Kara et al. 2005b). In contrast, it is clear from the results presented here that there are large differences in the accuracy of the seasonal SSH variability between the simulations assuming absorption of all radiation at the surface or using the clear water assumption, and the standard simulations using monthly mean turbidity fields from SeaWiFS.

7. Summary and conclusions

In this paper we examined the effects of water turbidity on the heat and buoyancy fluxes, mixed layer depth (MLD), sea surface height (SSH), and sea surface currents in the Black Sea using a Hybrid Coordinate Ocean Model (HYCOM) with ≈ 3.2 km resolution. A monthly mean attenuation of photosynthetically available radiation (k_{PAR}) climatology derived from the remotely sensed Sea-Viewing Wide Field-of-View Sensor (SeaWiFS) data during 1997–2001 is introduced for the Black Sea. It is then used for parameterization of the solar radiation penetration in HYCOM.

Six HYCOM simulations were performed with no assimilation of any oceanic data except initialization from climatology and relaxation to climatological sea surface salinity. These simulations use wind and thermal forcing from two different operational weather prediction models (ECMWF and NOGAPS). They are used to explain the importance of using spatial and temporal attenuation depths (experiments 1 and 4) as opposed to using a clear water constant solar attenuation depth (≈ 16.7 m) assumption (experiments 3 and 6) or absorption of all radiation at the sea surface (experiments 2 and 5). This was discussed in relation to MLD, SSH, and surface currents. The heat balance from the model simulations demonstrated that the net heat loss/gain at the sea surface was not small in winter/summer. Thus, penetrative solar radiation is the major component of the heat balance. Given that the mixed layer can be quite shallow (as shallow as 3 m) during the summer, accurate

parameterization of solar extinction using spatial and temporal solar attenuation depths is required in the Black Sea. Photosynthetic sensitivity to the spectral properties of shortwave solar radiation make it an even more important atmospheric forcing parameter for applications to biological productivity in the Black Sea.

Prediction of upper-ocean quantities from the model simulations clearly revealed that the dynamics of the mixed layer are quite sensitive to solar radiation attenuation. Ignoring the use of spatial and temporal attenuation depths in the model simulation results in some unrealistic features in the sea surface circulation on monthly time scales. This is due partly to the fact that stability of the upper ocean changes through the net buoyancy flux. The Black Sea, characterized by relatively weak stratification during winter, is not exposed to intense buoyancy loss to the atmosphere, implying that the convection does not usually mix surface waters to a great depth. The buoyancy is much more sensitive to variations in heating in the Black Sea. Thus, the heat flux determines most of the buoyancy fluctuations in all months except March on the climatological time scales. The main difference in basin-averaged MLD between experiments 1 and 3 (and similarly, between experiments 4 and 6) occurred in the winter and early spring. The model response to ECMWF or NOGAPS forcing generally yielded similar results, indicating the importance of using monthly mean k_{PAR} climatology in the model for realistic predictions of upper-ocean quantities.

Finally, a monthly mean SSH anomaly climatology based on satellite altimeter data was introduced for the Black Sea. Major goals of constructing the climatology were to 1) combine disparate satellite altimeter data types and irregular sampling patterns, so that spatial and temporal variability of SSH could be obtained, and 2) provide a climatology that can be used for model–data comparisons. The climatology was obtained from sea level data observed by three satellite altimeters using an optimal interpolation during 1993–2002. The model was tested against the monthly mean SSH anomaly climatology. For the seasonal cycle the basin-averaged rms differences between HYCOM SSH obtained from simulations that use spatially and monthly varying attenuation depths and the climatological SSH were 3.9 (experiment 1) and 3.7 cm (experiment 4). However, large SSH rms difference values exist when all radiation is absorbed at the sea surface in the model simulations (5.4 cm for experiment 2 and 5.3 cm for experiment 5), giving 38% and 43% increase in comparison to experiments 1 and 4, respectively, or using a constant clear water attenuation depth assumption (5.7 cm for experiment 3 and 5.9 cm for experiment 6), giving 46% and 59% increase in comparison to experiments 1 and 4. These results confirm that, given the small SSH anomaly variability in the Black Sea, neglecting spatial and temporal solar attenuation depth values in the model results in unrealistic SSH predictions.

APPENDIX

Symbol Definitions

a_s	constant coefficient of ϕ_s (-28.86)
$B(z)$	mean buoyancy profile (m s^{-2})
B_f	surface buoyancy forcing (m^2 s^{-3})
B_r	near-surface reference buoyancy (m s^{-2})
c_s	constant coefficient of ϕ_s (98.96)
C_v	ratio of interior N to N at h_e (a constant between 1 and 2)
C_w	specific heat of water (3990.5 J kg^{-1} K^{-1})
E	evaporation (m s^{-1})
f	Coriolis parameter (s^{-1})
f^+	f at 5°N latitude (2.5×10^{-5} s^{-1})
$\hat{f}$	maximum value of $\|f\|$ or f^+
g	gravitational acceleration (9.81 m s^{-2})
h_b	boundary layer depth (m)
h^*	stable depth (m)
h_e	entrainment depth (m)
h_e^*	Ekman depth (m)
$\mathbf{i}$	unit vector in x direction
$\mathbf{j}$	unit vector in y direction
$\mathbf{k}$	unit vector in z direction
L	Monin–Obukhov length (m)
M	Montgomery potential (m^2 s^{-2})
N	local buoyancy frequency (s^{-1})
p	barotropic pressure (N m^{-2})
P	precipitation (m s^{-1})
R	buoyancy ratio
Q_a	net heat flux at the sea surface (W m^{-2})
Ri_b	bulk Richardson number
Ri_c	critical Ri_b number (0.3)
s	generalized vertical coordinate
S	salinity (psu)
S_s	sea surface salinity (psu)
T	temperature (°C)
T_s	sea surface temperature (°C)
u	wind component in x direction (m s^{-1})
$\mathbf{u}$	horizontal velocity vector (m s^{-1})
u_*	turbulent friction velocity (m s^{-1})
υ	wind component in y direction (m s^{-1})
$\mathbf{v}(z)$	boundary layer horizontal velocity profile (m s^{-1})
$\mathbf{v}_r$	near-surface reference horizontal velocity vector (m s^{-1})
$V_t(z)$	unresolved turbulent velocity shear profile (m s^{-1})
t	time (s)
x	eastward distance (m)
w_s	turbulent velocity scale for T and S (m s^{-1})
w_*	convective velocity scale (m s^{-1})
y	northward distance (m)
z	depth from the surface (m)
α_p	potential specific volume (kg^{-1} m^3)
α_{pref}	reference value of α_p (1 kg^{-1} m^3)
$\alpha(T_s, S_s)$	thermal expansion coefficient (°C^{-1})
$\beta(T_s, S_s)$	salt expansion coefficient (psu^{-1})
β_T	ratio of entrainment flux to surface buoyancy flux (-0.2)
ε	nondimensional extent of the surface layer (0.1)
κ	von Kármán constant (0.4)
Ω	rotation rate of the earth (7.292×10^{-5} s^{-1})
ϕ	latitude (°)
ϕ_s	nondimensional flux profiles for scalars
ρ	density (kg m^{-3})
ρ_0	reference density (1000 kg m^{-3})
σ	nondimensional vertical coordinate in the boundary layer
σ_t	density ($\rho - 1000$ kg m^{-3})
τ	the wind- and/or bottom-drag induced shear stress vector (N m^{-2})
ζ	relative vorticity (s^{-1})

REFERENCES

Bleck, R., 2002: An oceanic general circulation model framed in hybrid isopycnic-cartesian coordinates. *Ocean Modell.,* **4,** 55–88.

Chassignet, E. P., L. T. Smith, G. R. Halliwell, and R. Bleck, 2003: North Atlantic simulations with the Hybrid Coordinate Ocean Model (HYCOM): Impact of the vertical coordinate choice, reference pressure, and thermobaricity. *J. Phys. Oceanogr.,* **33,** 2504–2526.

Daley, R., 1991: *Atmospheric Data Analysis.* Cambridge University Press, 457 pp.

Dynesius, M., and C. Nilsson, 1994: Fragmentation and flow regulation of river systems in the northern third of the world. *Science,* **266,** 753–762.

Fox, D. N., W. J. Teague, C. N. Barron, M. R. Carnes, and C. M. Lee, 2002: The Modular Ocean Data Assimilation System (MODAS). *J. Atmos. Oceanic Technol.,* **19,** 240–252.

Gibson, J. K., P. Kållberg, S. Uppala, A. Hernandez, A. Nomura, and E. Serrano, 1997: ERA description. ECMWF Re-Analysis Project Rep. Series 1, 72 pp. [Available from ECMWF, Shinfield Park, Reading RG2 9AX, United Kingdom.]

Halliwell, G. R., Jr., 2004: Evaluation of vertical coordinate and vertical mixing algorithms in the HYbrid Coordinate Ocean Model (HYCOM). *Ocean Modell.,* **7,** 285–322.

Jacobs, G. A., and J. L. Mitchell, 1997: Combining multiple altimeter missions. *J. Geophys. Res.,* **102,** 23 187–23 206.

——, C. N. Barron, and R. C. Rhodes, 2001: Mesoscale characteristics. *J. Geophys. Res.,* **106,** 19 581–19 595.

Jerlov, N. G., 1976: *Marine Optics.* Elsevier Oceanography Series, Vol. 14, Elsevier, 231 pp.

Kara, A. B., P. A. Rochford, and H. E. Hurlburt, 2000: An optimal definition for ocean mixed layer depth. *J. Geophys. Res.,* **105,** 16 803–16 821.

——, ——, and ——, 2002: Air–sea flux estimates and the 1997–1998 ENSO event. *Bound.-Layer Meteor.,* **103,** 439–458.

——, ——, and ——, 2003a: Mixed layer depth variability over the global ocean. *J. Geophys. Res.,* **108,** 3079, doi:10.1029/2000JC000736.

——, A. J. Wallcraft, and H. E. Hurlburt, 2003b: Climatological SST and MLD simulations from NLOM with an embedded mixed layer. *J. Atmos. Oceanic Technol.,* **20,** 1616–1632.

——, H. E. Hurlburt, P. A. Rochford, and J. J. O'Brien, 2004: The impact of water turbidity on the interannual sea surface temperature simulations in a layered global ocean model. *J. Phys. Oceanogr.,* **34,** 345–359.

——, A. J. Wallcraft, and H. E. Hurlburt, 2005a: A new solar radiation penetration scheme for use in ocean mixed layer studies: An application to the Black Sea using a fine resolution Hybrid Coordinate Ocean Model (HYCOM). *J. Phys. Oceanogr.,* **35,** 13–22.

——, ——, and ——, 2005b: Sea surface temperature sensitivity to water turbidity from simulations of the turbid Black Sea using HYCOM. *J. Phys. Oceanogr.,* **35,** 33–54.

Kempe, S., M. Pettine, and G. Cauwet, 1991: Biogeochemistry of European rivers. *Biogeochemistry of Major World Rivers,* E. T. Degens, S. Kempe, and J. E. Richey, Eds., John Wiley, 356 pp.

Korotaev, G. K., V. A. Saenko, C. J. Koblinsky, and V. V. Knysh, 1998: Study of the Black Sea circulation using Topex–Poseidon altimetry. *Earth Res. Space,* **3,** 3–17.

Lalli, C. M., and T. R. Parsons, 1997: *Biological Oceanography: An Introduction.* Butterworth-Heinemann, 314 pp.

Large, W. G., G. Danabasoglu, S. C. Doney, and J. C. McWilliams, 1997: Sensitivity to surface forcing and boundary layer mixing in a global ocean model: Annual mean climatology. *J. Phys. Oceanogr.,* **27,** 2418–2447.

Marshall, J., and F. Schott, 1999: Open-ocean convection: Observations, theory, and models. *Rev. Geophys.,* **37,** 1–64.

McClain, C. R., M. L. Cleave, G. C. Feldman, W. W. Gregg, S. B. Hooker, and N. Kuring, 1998: Science quality SeaWiFS data for global biosphere research. *Sea Technol.,* **39,** 10–16.

Meybeck, M., 1988: How to establish and use world budgets of riverine materials. *Physical and Chemical Weathering in Geochemical Cycles,* A. Lerman and M. Meybeck, Eds., Kluwer Academic, 247–272.

Millero, F. J., and A. Poisson, 1981: International one-atmosphere equation of state of seawater. *Deep-Sea Res.,* **28A,** 625–629.

——, C.-T. Chen, A. Bradshaw, and K. Schleicher, 1980: A new high pressure equation of state for seawater. *Deep-Sea Res.,* **27A,** 255–264.

Milliman, J. D., and R. H. Meade, 1983: World-wide delivery of river sediments to the oceans. *J. Geol.,* **91,** 1–21.

Oguz, T., and P. Malanotte-Rizzoli, 1996: Seasonal variability of wind and thermohaline driven circulation in the Black Sea: Modeling studies. *J. Geophys. Res.,* **101,** 16 551–16 569.

——, and S. Besiktepe, 1999: Observations on the Rim Current structure, CIW formation and transport in the Western Black Sea. *Deep-Sea Res.,* **46A,** 1733–1753.

——, H. W. Ducklow, and P. Malanotte-Rizzoli, 2000: Modeling distinct vertical biogeochemical structure of the Black Sea: Dynamical coupling of the oxic, suboxic, and anoxic layers. *Global Biogeochem. Cycles,* **14,** 1331–1352.

Perry, G. D., P. B. Duffy, and N. L. Miller, 1996: An extended data set of river discharges for validation of general circulation models. *J. Geophys. Res.,* **101,** 21 339–21 349.

Rosmond, T. E., J. Teixeira, M. Peng, T. F. Hogan, and R. Pauley, 2002: Navy Operational Global Atmospheric Prediction System (NOGAPS): Forcing for ocean models. *Oceanography,* **15,** 99–108.

Stanev, E. V., and J. V. Staneva, 2001: The sensitivity of the heat exchange at sea surface to meso and sub-basin scale eddies: Model study for the Black Sea. *Dyn. Atmos. Oceans,* **33,** 163–189.

Staneva, J. V., D. E. Dietrich, E. V. Stanev, and M. J. Bowman, 2001: Rim Current and coastal eddy mechanisms in an eddy-resolving Black Sea general circulation. *J. Mar. Syst.,* **31,** 137–157.

Vörösmarty, C. J., K. Sharma, B. M. Fekete, A. H. Copeland, J. Holden, J. Marble, and J. A. Lough, 1997: The storage and aging of continental runoff in large reservoir systems of the world. *Ambio,* **26,** 210–219.

Wallcraft, A. J., A. B. Kara, H. E. Hurlburt, and P. A. Rochford, 2003: The NRL Layered Global Ocean Model (NLOM) with an embedded mixed layer submodel: Formulation and tuning. *J. Atmos. Oceanic Technol.,* **20,** 1601–1615.

Yuen, C. W., J. Y. Cherniawsky, C. A. Lin, and L. A. Mysak, 1992: An upper ocean general circulation model for climate studies: Global simulation with seasonal cycle. *Climate Dyn.,* **7,** 1–18.

Zaneveld, J. R. V., J. C. Kitchen, and J. L. Müeller, 1993: Vertical structure of productivity and its vertical integration as derived from remotely sensed observations. *Limnol. Oceanogr.,* **38,** 1384–1393.

Zatsepin, A. G., A. I. Ginzburg, A. G. Kostianoy, V. V. Kremenetskiy, V. G. Krivosheya, S. V. Stanichny, and P.-M. Poulain, 2003: Observations of Black Sea mesoscale eddies and associated horizontal mixing. *J. Geophys. Res.,* **108,** 3246, doi:10.1029/2002JC001390.